Prabha Materials Science Letters
Vol. 3, No. 1, 146-174, 2024
https://doi.org/10.33889/PMSL.2024.3.1.010

Ram Arti Publishers

Experimental Techniques for the Characterization of Magnetic Thin Films

Amit Kumar Singh
Department of Physics,
Marwari College, Lalit Narayan Mithila University, Darbhanga, 846004, Bihar, India.
Corresponding author: amitphy1991@gmail.com

Ashwani Kumar
Department of Physics,
Regional Institute of Education (NCERT), Bhubaneswar, 751022, Odisha, India.
E-mail: 01ashraj@gmail.com

(Received on January 27, 2024; Revised on March 31, 2024; Accepted on March 31, 2024)

Abstract
This review article describes the various experimental techniques, which are required for the characterization of magnetic thin films. Characterization is an essential process to understand the properties of magnetic thin films. By knowing the properties of these materials, one can utilize them in various technological applications as per requirements. There are different characterization tools to study the different properties of nanostructured materials. Some important experimental techniques employed to characterize the magnetic thin films are: X-Ray Diffraction, X-Ray reflectivity, Field emission scanning electron microscopy, Energy dispersive spectrometer, Transmission electron microscopy, Superconducting quantum interference device, Raman spectroscopy and X-ray absorption spectroscopy etc. These techniques will develop a better understanding of the structural, morphological, and magnetic properties of the materials to the scientific community. The discussion made in the present review article would be extremely helpful to the researchers who are doing research in the various branches of science and engineering.

Keywords- Nanomaterial, XRD, FE-SEM, SQUID, Raman spectroscopy, XAS.

1. Introduction

Thin film technology is an emerging field that includes almost every discipline of science and engineering (Gajek et al., 2005; Narayan, 2005; Cui et al., 2013; Singh et al., 2017a; Tyagi et al., 2021). In the simplest words, a thin film can be defined as a layer of a material with thickness in the range of nanometers or fractions of micrometers. The ever-increasing demand of miniaturization in magnetic recording media, with advances in thin film synthesis techniques, has accelerated the investigation of thin films of different materials (Venimadhav et al., 2004; Venimadhav et al., 2005; Ghimpu et al., 2013; Yadav and Chaudhary, 2015a, 2015b). The applications of thin films are countless as they are now involved in almost every aspect of the physical world (Bajaj et al., 2007a, 2007b; Singh et al., 2007; Kumar et al., 2008; Sofin et al., 2011; Raju et al., 2013; Rana et al., 2013; Kamerbeek et al., 2014; Low et al., 2014; Husain et al., 2017). From the household mirror to a computer memory or a solar cell, thin films are widely used for their multiple advantages in different ways. Growth of thin film onto an appropriate substrate depends on the surface energy of both the depositing material as well as the substrate used (Ohring, 1992). Nucleation and agglomeration processes for the depositing material depend upon the type of substrate. Nucleation process on the surface of a substrate takes place when an atom or ion transfer a part or whole of its kinetic energy to the substrate, thus helping it to get adsorbed onto the surface of the substrate. This process results in the adsorption of the atoms or adatoms to the substrate either via Vander-Waals or via covalent forces (Ohring, 1992).

However, the adsorption of atoms takes place when the residual kinetic energy of these adsorbed atoms is higher than the binding forces. Only in that condition, the atoms get diffused onto the surface of substrate or might get form gas phase by desorption from the surface. During this process, the diffused atoms keep moving surrounding the surface depending upon the loss of energy or come across a state where the binding effects are resilient to pin them down. Moreover, the mobility of the diffused atoms may exist for a long period of the order of several seconds depending on their surface energy. Surface defects like grain boundaries, step edges, or surface impurities are the common regions where these diffused atoms will get trapped. These bound adatoms then themselves become the points for binding other diffusing adatoms for the nucleation of grains. The nucleation process results in the formation of crystallites or grains. The properties of the thin film of a given material depend on the microstructure of the films, which further depends on deposition parameters and the substrate material. It is a well-known fact that when a bulk material transforms into a thin film, then one can observe significant changes in the physical properties of the thin film than its bulk counterpart. These properties of thin films can be easily applied to the device application. The applications of thin film in various fields have grown rapidly with time. Now-a-days, they have become a vital part of both industrial and research purposes. The thin films can have a thickness ranging from a few tenths of a nanometer to a few micrometers. Thin film is a very fascinating area of research and application. The applications of thin film can be classified into the following categories: optics, magnetic, optoelectronics, sensors, biomedicine, energy storage, and fuel cells etc. Figure 1 shows the main area where thin film technology is very important.

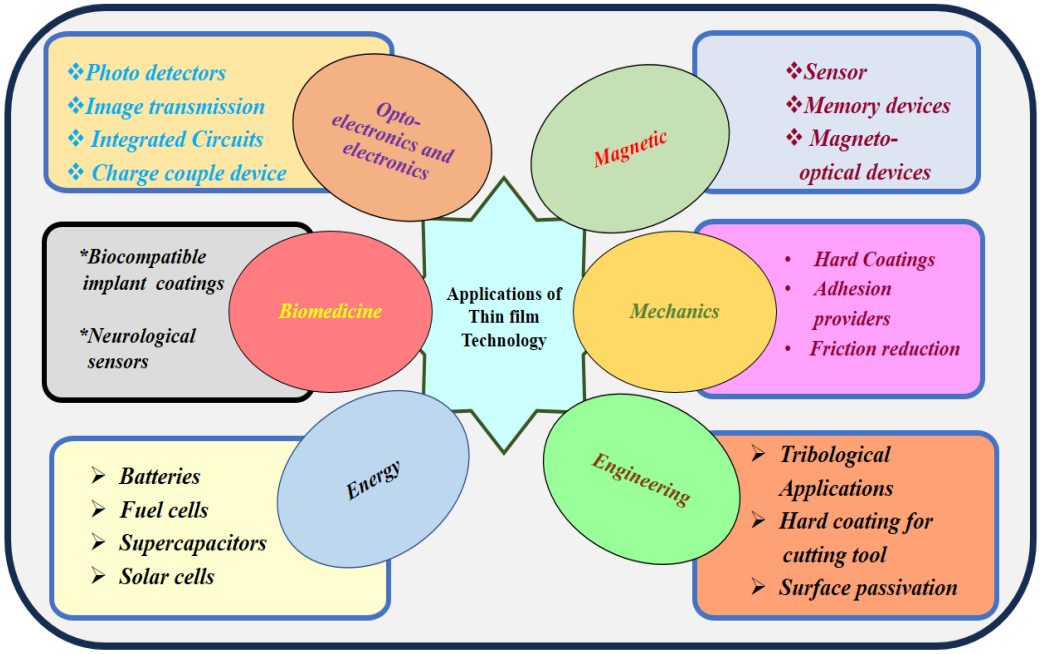

Figure 1. Schematic diagram for the applications of thin film technology.

Among them, magnetic thin film can be considered as a potential candidate to construct the different devices with improved performance. Synthesis of highly crystalline magnetic thin films with desired dimensions and homogeneity is essential for device applications (Mishra et al., 2014; Singh et al., 2017a; Singh et al. 2017b; Singh et al., 2017c). The fabrication of such type of high quality magnetic thin films will be helpful in the development of spintronic devices. The improved properties of such magnetic thin films can be measured by means of some characterization techniques. Thus, the study of sophisticated characterization

techniques is necessary to synthesize the materials in Nano dimension with better crystallinity and morphology (Khan et al., 2019). Therefore, it is essential for scientific community to understand the basic principle, construction, and operation of characterization techniques in detail. In this regard, we have made an attempt to discuss the various characterization techniques that are useful in determining the different properties of magnetic thin films. Thus, the discussion made in this article would be helpful for the researchers in doing the systematic study of magnetic thin films.

2. Characterization Techniques

2.1 X-Ray Diffraction

X-Ray diffraction is considered as the most extensively utilized non-destructive technique for the identification of crystal structure, phase, orientation, lattice parameters and stress in a crystalline material (Cullity, 1956; Bunaciu et al., 2015; Ali et al., 2022). X-Rays fall into the category of electromagnetic radiations having wavelength ranging from 0.01 to 10 nm. X-Ray diffraction results from the interference of diffracted beams of a monochromatic X-Ray source which are incident on a crystalline structure. Periodically arranged atoms in the crystal can be regarded as scattering centers for X-Rays. X-Ray radiations can be simply diffracted by atomic planes, since their order (few Å) of wavelength is equal or comparable to the inter-planar spacing between the nearby atomic planes (Cullity, 1956). Diffraction takes place between the waves when they encounter an obstacle whose size is comparable to their wavelength.

If we consider a crystal structure with periodic arrangement of atoms as shown in Figure 2, then there are two geometrical factors which are to be considered: firstly, the incident beam, at right angles to the diffracting plane and the diffracted beam, all exists in a same plane, and secondly, the angle amid the incident and the diffracted beam (2θ), which is the diffraction angle usually measured experimentally.

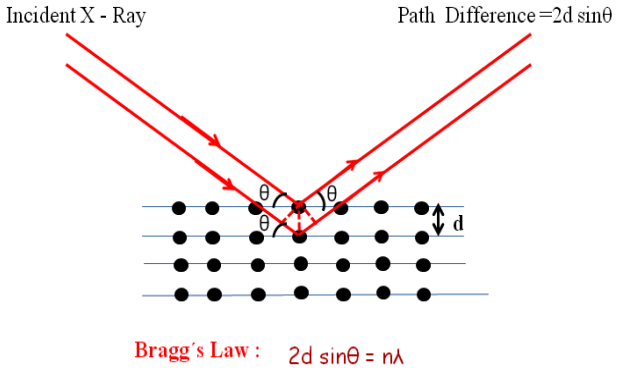

Figure 2. Schematic diagram for X-Ray diffraction from a crystal.

For an incident X-ray falling on a periodic structure making an angle θ with the plane, constructive interference for planes of the crystalline structure parallel to the sample plane takes place when the following condition is fulfilled:

$$2d \sin\theta = n\lambda \quad (1)$$

Here, d is the spacing between the adjacent planes, λ is the wavelength of the incoming X-ray and n is the integers (n = 1, 2, 3…). This equation for the diffraction of X-rays from atomic planes is designated as Bragg's Law. Since, the largest value of sin θ could be 1. Therefore, $\frac{n\lambda}{2d} < 1$, and hence, $n\lambda << 2d$. The smallest possible value of n is 1, so $\lambda < 2d$. Since, for large number of crystal planes d is comparable or less

than 3 Å, therefore, the λ of the incoming radiation should be less than 6 Å. X-rays whose wavelength is of the order of few Å, are suitable for resolving the spacing between the atomic planes in common oxides or metals which is also of the order of few Å. The crystallographic information of a material can be attained by calculating the *d* values and indexing the reflections obtained from the diffraction pattern. The characteristic diffraction pattern of a material is achievable irrespective of the material state; available in pure state or exists in a mixture of other materials (Ameh, 2019; Khan et al., 2020). In this regard, the diffraction method is an ideal tool for pre-recognition of the materials phase (Cullity, 1956). The X-ray diffraction pattern is analyzed with a 2θ value and relative intensities (I) gives information about the presence of specific phase.

XRD is an essential technique for the phase analysis (Bunaciu et al., 2015; Ameh, 2019; Khan et al., 2020; Ali et al., 2022). For instance, Singh et al. (2017b), synthesized Nd_2NiMnO_6 (NNMO) thin films on (001) oriented STO substrate with varying thickness. The thicknesses of the samples were 60, 90, 180, 240 and 300 nm, which were marked as samples S1, S2, S3, S4 and S5, respectively.

X-Ray diffraction curves for all the films are depicted in Figure 3. They observed only (00*l*) reflections for all the films along with the reflections for substrate. They represented the additional two peaks by K_β and W which were the resultant of (00*l*) K_β reflection and tungsten impurities in X-ray beam. Moreover, they found some significant peaks (marked as *) in the XRD patterns corresponding to the bare substrate. There did not find any extra impurity peak in the XRD patterns.

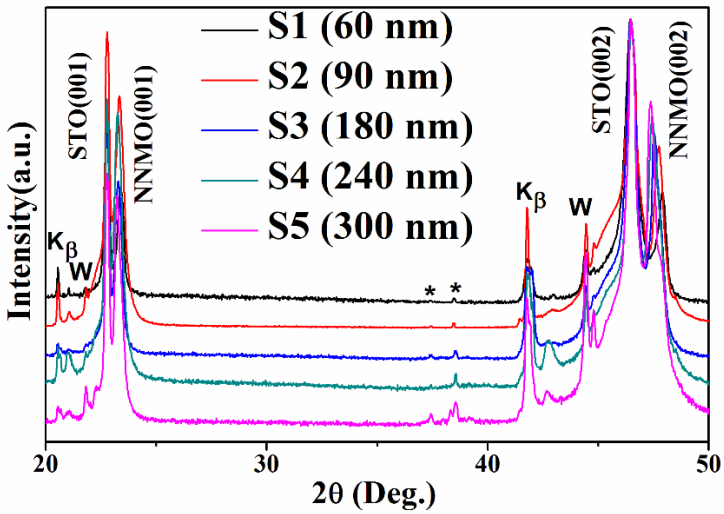

Figure 3. X-ray diffraction pattern of NNMO films with various thickness [with the copyright permission of reference (Singh et al., 2017b)].

Figure 4 shows the sketch of all the angles involved in an X-Ray diffraction measurement. Here, Ψ represents tilt of the sample, φ corresponds to the in-plane rotation and ω is the angle between the atomic plane of the specimen and the X-ray tube. For all the samples, whether in powdered form, pellet form or thin film, the measurements are done in locked coupled arrangement. In this arrangement, the tube and detector move simultaneously to cover the whole 2θ range (say 5 - 90°). This arrangement is therefore known as θ-θ scan. Thus, angle ω, between the tube and the sample surface, and θ between the detector and the sample surface always remain same during the scan.

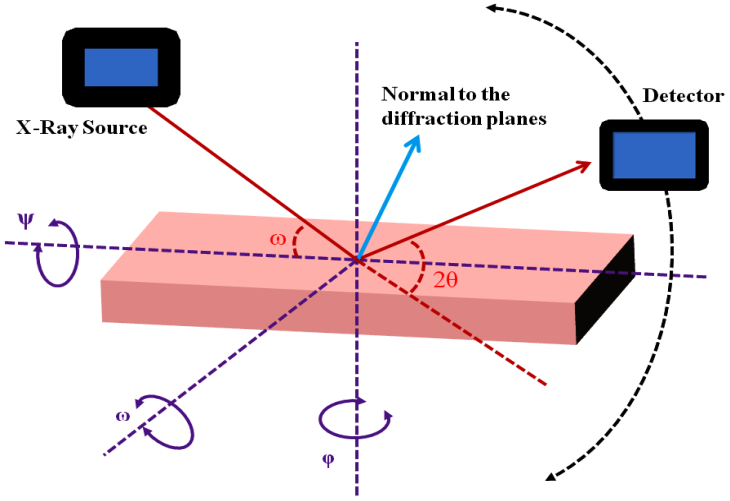

Figure 4. Schematic representation of the angles involved in X-Ray diffraction of a sample.

For the characterization of thin films, the rotation is given to the sample holder, so that, the reflections from all the diffracting planes could be recorded by the detector. The detector consists of a NaI scintillation counter which can detect the diffracted beam having wavelength in the range of 0.5 -3 Å. The peaks obtained in the diffraction pattern can then be indexed to recognize the phase formation and to estimate the lattice constants and particle size from peaks' angle and their FWHM.

XRD technique can also be utilized to determine the epitaxial nature of thin film. In a study (Singh et al., 2017c), NNMO thin films were grown on (001) oriented different substrates viz. LAO, STO and LSAT substrates (denoted by NNMO/LAO, NNMO/STO and NNMO/LSAT, respectively). From the X-ray diffraction scan in θ-2θ geometry, they observed the (00*l*) Bragg peaks of the NNMO films close to that of the substrate peaks (Figure 5(a-c)). The appearance of only one peak with small FWHM in the rocking scans (shown in the insets of Figure 5(a-c)) indicates the growth of thin films in a coherent and epitaxial mode. They also showed the Φ scan of in-plane (200) reflection of NNMO/STO film in Figure 5 (d). The appearance of peaks at repeated interval signifies the epitaxial growth of thin film.

Further, the angular position of lines directly hinges on the λ of the incident X-ray and interplanar spacing (*d*) of the lattice planes. The quantitative analysis of the materials phases can be done via evaluating the area under peak. The intensity of peaks mainly relays on the amount of the sample materials in the specimen. The qualitative analysis of the material is performed via the identification of the diffraction pattern of the material, respectively. The crystallite size is on the major parameter used for analysis of the nanomaterials and can be calculated using the Scherrer's equation (Cullity, 1956):

$$D = \frac{0.9\,\lambda}{\beta\,\cos\theta} \qquad (2)$$

where, λ - wavelength, β is the full width at half maxima (FWHM) of the Bragg peak after instrumental correction in the peak broadening, and 2θ is the Bragg angle. In order to find the exact broadening of peak because of small particle size, subtraction of the instrumental contribution from the observed peak width is necessary.

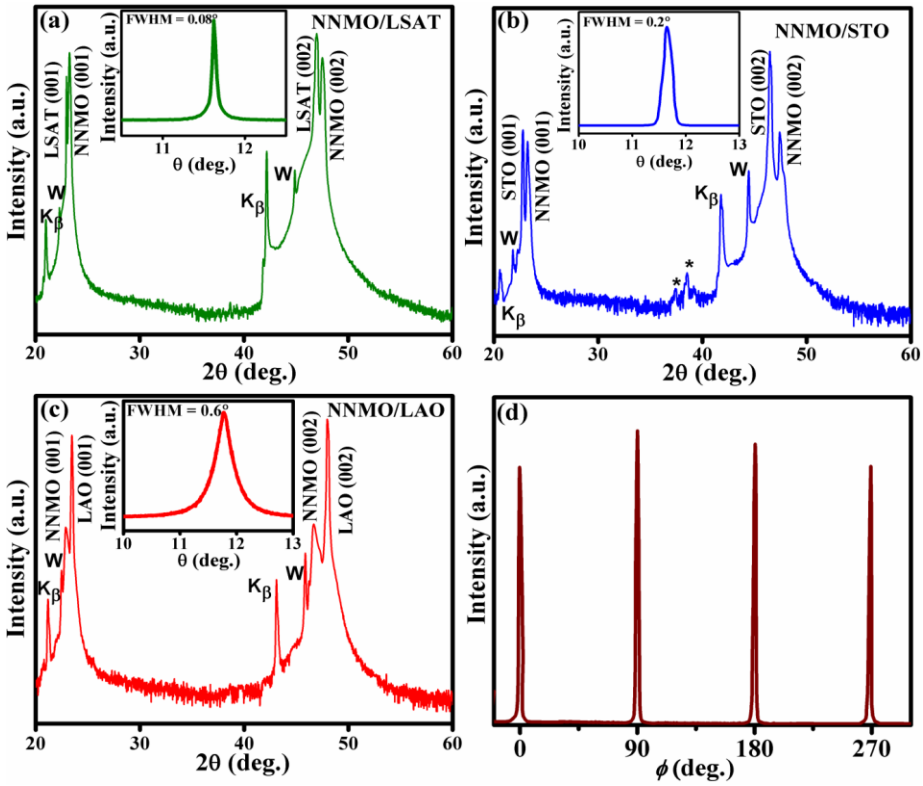

Figure 5. (a-c) X-Ray diffraction (θ-2θ) patterns for NNMO thin films grown on different substrates: (a) LSAT, (b) STO, and (c) LAO. The insets are the rocking curves of the films. (d) shows the Φ scan of in-plane (200) reflection of NNMO/STO film. [with the copyright permission of reference (Singh et al., 2017c)]

2.2 X-Ray Reflectivity

X-Ray reflectivity (XRR) measurement can be performed using X-Ray Diffractometer to estimate the thickness of the thin films when the thickness lies in a range of 10-300 nm and their surface and interface roughness is not too large (Yasaka, 2010; Islam et al., 2020; Verna et al., 2021). In this measurement, the incident X-ray strikes the surface of the film at very low incidence angle θ_i (grazing angle) as depicted in Figure 6. The detector is placed with an angle $\theta_d = \theta_i$. When incidence angle just surpasses the critical angle θ_c of the thin film material, then, part of the incident X-ray is reflected (R) and part of it is diffracted and comes out again (D). Both the beams (I and R) are parallel and produce interference depending upon the path travelled by the beam D inside the film.

Some XRR patterns are shown in Figure 7 and Figure 8, the periodicity of the fringes or oscillations in the pattern decides the thickness of the film. The oscillations occur due to interference between the beams I and D. The film thickness was measured using the following formula (Yasaka, 2010):

$$d = \frac{2\pi}{\Delta q} \quad (3)$$

$$q = \frac{4\pi}{\lambda} \sin\theta \quad (4)$$

$$d = \frac{\lambda}{2(\sin\theta_2 - \sin\theta_1)} \quad (5)$$

Here, θ is the angle corresponding to the maxima in the oscillation.

In the study, which is also discussed in the XRD section, NNMO thin films were grown by Singh et al. (Singh et al., 2017b) onto STO substrate with varying thickness. They employed the low angle X-Ray reflectometry (XRR) to estimate the thickness of each sample. The XRR patterns were shown in Figure 7. The thicknesses were found to be 60, 90, 180, 240 and 300 nm for the samples S1, S2, S3, S4 and S5, respectively.

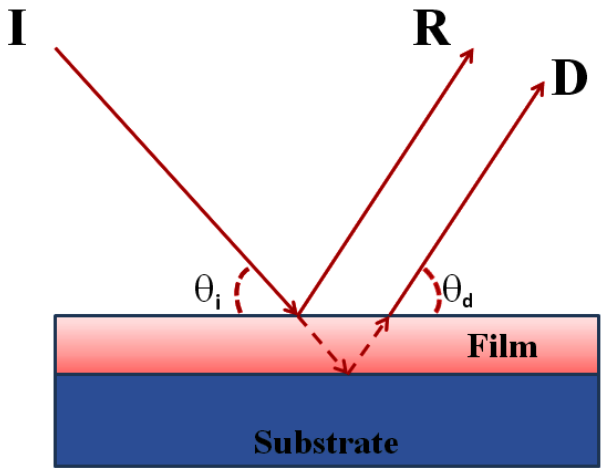

Figure 6. Schematic diagram of X-Ray reflectivity.

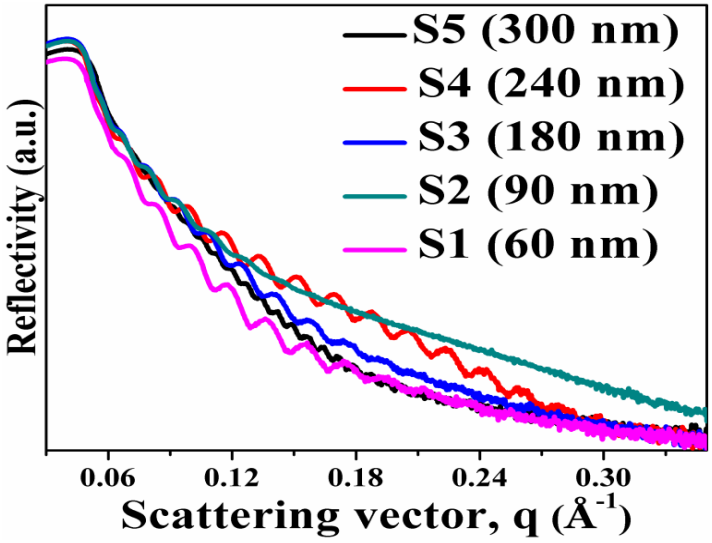

Figure 7. XRR scan curves of NNMO films [with the copyright permission of reference (Singh et al., 2017b)].

In another study, La_2NiMnO_6 (LNMO), $LaMnO_3$ (LMO) and $[LNMO/LMO]_{15}$ multilayers were deposited by Singh and Chandra (2018) on (001) $LaAlO_3$ substrate. The XRR pattern of these samples were shown in Figure 8. The repetition of different type patterned fringes after a regular interval signifies the presence of two different types of material within a sample in a repetitive manner.

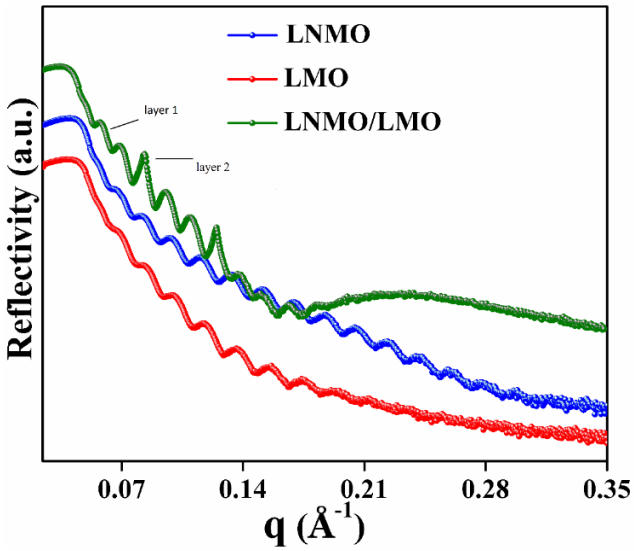

Figure 8. XRR patterns of LMO, LNMO and LNMO/LMO multilayers deposited on LAO substrate.

2.3 Field Emission Scanning Electron Microscopy

Field emission scanning electron microscopy (FE-SEM) is a versatile technique for studying the morphology and microstructure of materials (Mazzaglia et al., 2009). Before going into details of FE-SEM technique, a brief description of the interaction between an electron and matter is given. When an electron beam strikes a specimen, it may exhibit an interaction with the atoms of the specimen in various means deciding by its energy (Figure 9). These interactions of electron with matter can be categorized into two main classes: elastic and inelastic scattering (Goodhew et al., 2001).

(i) *Elastic Scattering:* Elastic scattering results from Coulombic interactions between the primary electron (incident electron) and the nucleus and electrons of the atoms of specimen. Elastic scattering changes the direction of the primary electron without changing its energy. This is also known as Rutherford scattering and gives a strong forward peaked distribution of scattered electrons. Elastic scattering is important for electron microscopy as a large number of electrons are deflected by this mechanism and also are main contributors for diffraction patterns.

(ii) *Inelastic Interactions:* Inelastic scattering causes the primary electron to lose a detectable amount of energy as it collides with another electron or nucleus of the atom. The loss in the electron's energy should be more than 0.1 eV before it could be detected. There are many ways in which the primary electron could lose its energy and transfer it to another electron or atom of the specimen. Inelastic scattering could result in the stopping of an electron by a solid, so that almost all the kinetic energy of the primary electron will result in heating of the sample. A slight proportion of the energy of the primary electron could give rise to X-rays, light or secondary electrons which prove to be beneficial for imaging and analysis (Ali et al., 2023).

Secondary Effects: Secondary effects are those effects caused by the primary electrons which could be detected outside the specimen. The secondary effects are divided into following main categories (Inkson, 2016):

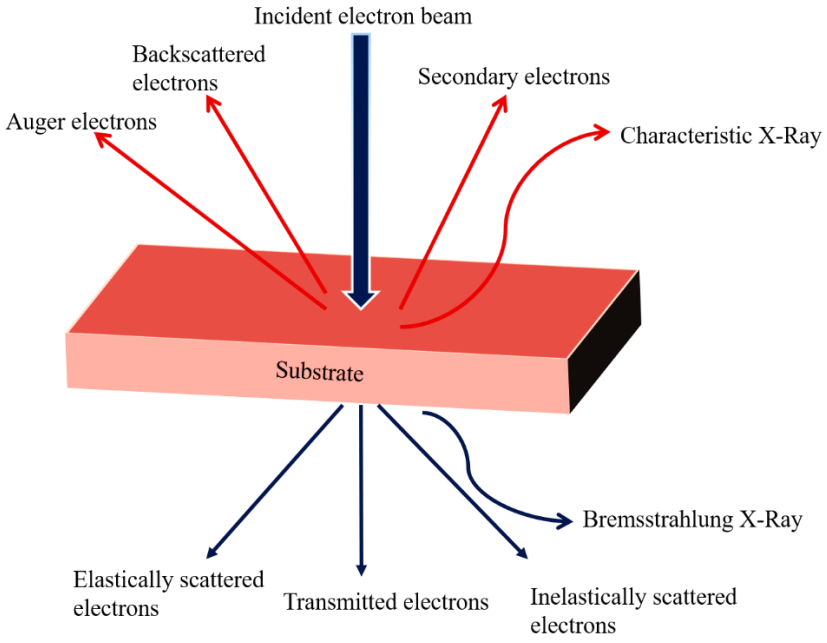

Figure 9. Schematic diagram for the signals acquired from the interaction of electrons with matter.

(i) *Secondary Electrons*: Those electrons which outflow from the sample with energy below ~50 eV is categorized as secondary electrons. Secondary electrons could be the primary electrons those have lost most of the energy inside the specimen and comes out of the specimen with remaining little energy of few eV. A small amount of energy could also be transferred to them (inelastic scattering) within a few distance of the sample surface. The secondary electron yield means the number of secondary electrons produced over each primary electron could be equal to or greater than 1. Secondary electrons are therefore plentiful and are the most useful one for imaging purpose in scanning electron microscopes (Mourdikoudis et al., 2018).

(ii) *Backscattered Electrons*: Those electrons which come out of the specimen surface without losing significant amount of their energy. Backscattered electrons are not as large in number as secondary electrons but most of them carry high energy and are useful for imaging, diffraction, and analysis in SEM (Ali et al., 2023).

(iii) *Relaxation of Excited Atoms*: When a localized electron comes out from an atom due to the interaction with the primary electron, the atom will go into an excited state. When this empty state is filled by another electron, the atom will relax and the excess energy will result into a secondary effect. This relaxation of the atom could happen in three possible ways. When the vacant electron state is in the outermost shell of the atom, a very less amount of energy is released which could be in the form of photons lying in the visible range. This phenomenon is known as *cathodoluminescence*. However, when the vacant state lies in the inner shell of the atom, larger amount of energy is released which could result into two possible effects: *characteristic X-Ray* or *characteristic Auger electron* (Goldstein et al., 2014). X-Rays are released when a single electron from the outer shell occupies the vacant state and the energy of these X-rays is the variance in energy among the two shells that is a characteristic of the particular atom. The element present in the specimen can be determined by calculating this energy. This forms the basis of analytical electron microscopy. However, if the primary electrons eject out an outer shell electron carrying the excess energy as its kinetic energy, then this phenomenon is called *Auger emission*. Three kinds of electrons are involved

in this process: the original vacancy, the outer electron which fills this vacancy and another outer electron which comes out after gaining the excess energy. The estimation of the energy of these Auger electrons forms the foundation of Auger electron microscopy (Mourdikoudis et al., 2018).

After having the information about how the electron interacts with a specimen, the details of a SEM are now discussed. A SEM is basically employed to examine the surface morphology of a specimen. Figure 10 exhibits the schematic of main apparatus and the procedure mode of a simple SEM (Goodhew et al., 2001). In a FE-SEM, field emission is employed to generate the electrons. In this case, a metal is brought into contact with a high electric field (>10^9 V/m), which is further responsible for the ejection of electrons from the metal surface. The effect is known as tunneling of electrons. In this process, many electrons are ejected from the tungsten source as compared to thermionic emission, resulting higher brightness (Mourdikoudis et al., 2018). A sharp tip is made of tungsten whose diameter is ~0.1μm, and acts as an emitter so that such a high electric field can be applied. Ultra-high vacuum (<10^{-7} Pa) is required in the gun to preserve such a delicate assembly. The main advantage of field-emission gun over thermionic gun is that the energies are very well defined with a very small energy spread (lower than 0.5 eV). Thus, the field-emission sources provide high brightness and monochromatic supply of electrons resulting electron microscopy with high resolution. The released electrons are then accelerated up to a voltage between 1keV to 30 keV. A fine electron beam with diameter of 2-10 nm is produced by passing accelerated electron beam through a series of condenser and objective lenses. The first condenser lens and aperture work in combination and helps in making the electron beam narrow by limiting its current. The second condenser lens then helps in making the electron beam finer and more coherent. The beam after going through the objective lens emphases onto the specimen (Goodhew et al., 2001).

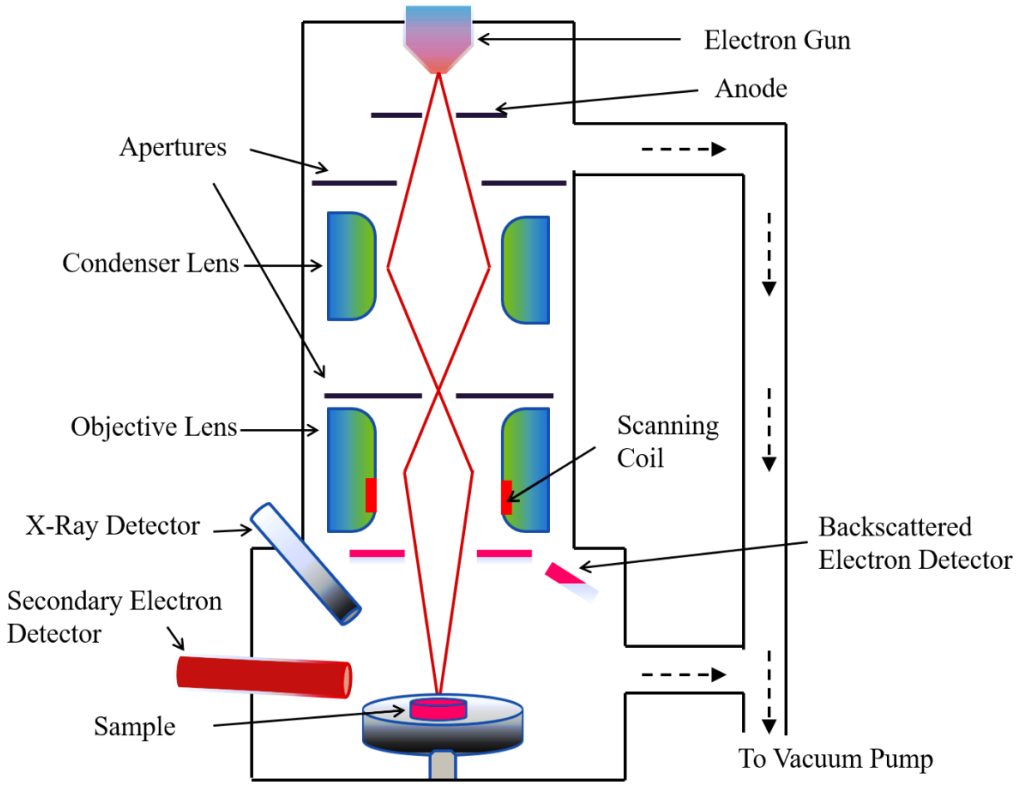

Figure 10. Schematic diagram of a Field-emission scanning electron microscope.

The electron beam then permits via a number of apertures which modify the properties of the current. After that, the electron beam passes through the scan coils which deflect the beam and helps in rastering the beam focus over the sample surface. The electron beam performs rastering pattern on the sample from left to right and top-to-bottom. There is a direct communication between the rastering pattern on the sample and the rastering pattern which produces the image on the computer. The resolution of the image depends upon the number of pixels in a row and the number of rows that consist of the examined area of the specimen. When an electron beam makes an interaction with the specimen, the ejection of secondary and backscattered electrons takes place (Delvallée et al., 2015). These electrons act as signals and are detected by the detectors. Secondary electrons are accumulated by the scintillator-photomultiplier system known as Everhart-Thornley detector. The Everhart-Thornley detector is very efficient for flat specimens and collects almost all the secondary electrons ejected from the surface of the sample.

In the aforesaid study (Singh et al., 2017b), which is also discussed in XRD and XRR section, the surface morphological analysis of the thin films was done by FE-SEM (Figure 11(a-e)). They observed from that all the films possess identical grain distribution throughout the surface of the films. They also saw that grains had regular shapes and sizes. They also reported that the size of grain increases with increasing film thickness. The thickness of the deposited thin films was also verified by them using cross-sectional FE-SEM image of sample S5, which is shown in Figure 11 (f). The estimated thickness was ~310 nm.

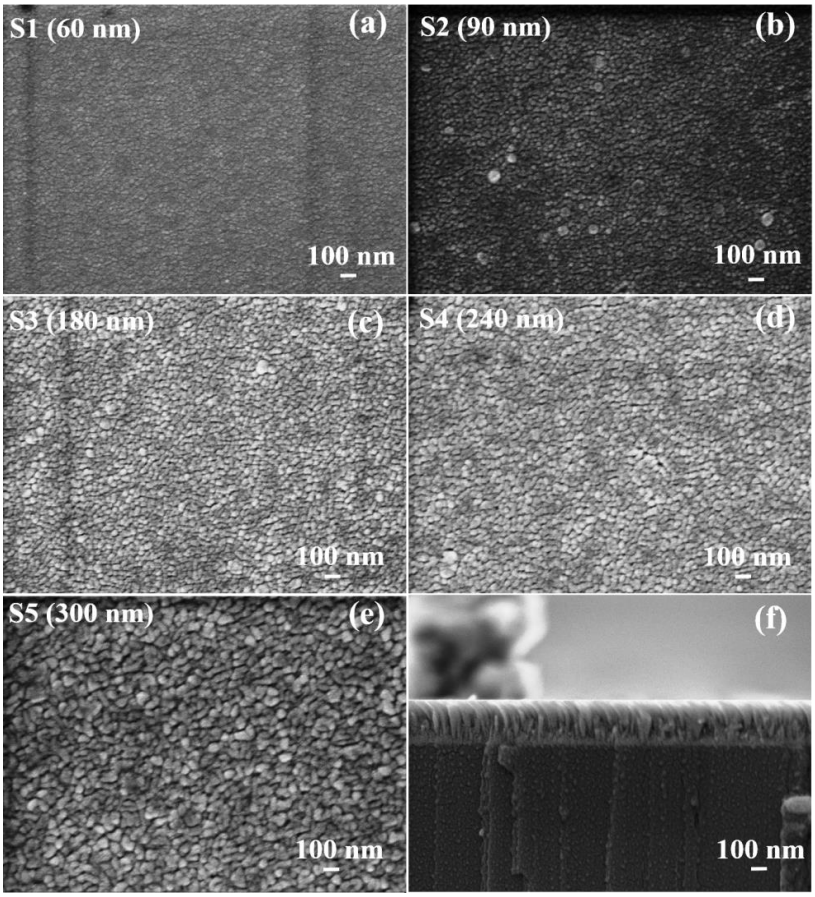

Figure 11. (a-e) FE-SEM images of thin films. (f) Cross-sectional FE-SEM image of 300 nm thick film [with the copyright permission of Reference (Singh et al., 2017b)].

2.4 Energy Dispersive Spectrometer

Element analysis can be performed using the energy dispersive spectrometer (EDS) coupled with the FE-SEM system (Scimeca et al., 2018). Several peaks obtain in EDS spectrum corresponds to the energy levels refer to the maximum received X-rays. Each peak in the EDS spectrum refers to a specific atom, and thus significant to identify single element. The spectrum with peak higher in intensity signifies the higher percentage of the element in the sample. The working principle of EDS is explained below:

X-Rays released from the sample surface are characteristic of the atoms of the specimen. Any element can be identified by its X-ray spectrum. Hence, the X-Rays can be employed for detecting of the elements existence in the specimen (Goodhew et al., 2001). The detector in EDS is a semiconducting Silicon or Germanium crystal positioned in a manner that it can detect most of the X-Rays released from the sample. Since X-Rays cannot be deflected, therefore, the detector should be aligned with the specimen and hence occupies same position to the secondary electron detector. When the X-Rays strike the detector, the electrons are excited to the conduction band leaving same number of holes in the outer shell. The amount of energy required for this is only 3.8 eV. Several electron-hole pairs produced is therefore related to the energy of X-Rays being emitted. A voltage is then applied across the semiconductor results in the flow of current as all X-rays are absorbed by the detector, the amount of this current is thus proportional to the X-rays' energy. For applying bias potential, the outer surface of the detector is coated with gold. Further, a Beryllium (Be) window is used to protect this gold –coated outer surface, preventing the impurities from the chamber to get deposited on the cold surface of the detector. Unfortunately, the Be window significantly absorbs low energy X-Rays and therefore makes it difficult to detect lighter elements. The current flow between the electrodes as the X-rays strike the detector for very short period, called as a pulse. This pulse is then amplified and passed to a multichannel analyzer (MCA) which decides the channel for the pulse (Each channel represents a different X-ray energy). The MCA thus collects the histogram of the energies of all X-rays received by the detector and produces the final data in the form of a smooth curve on the computer screen.

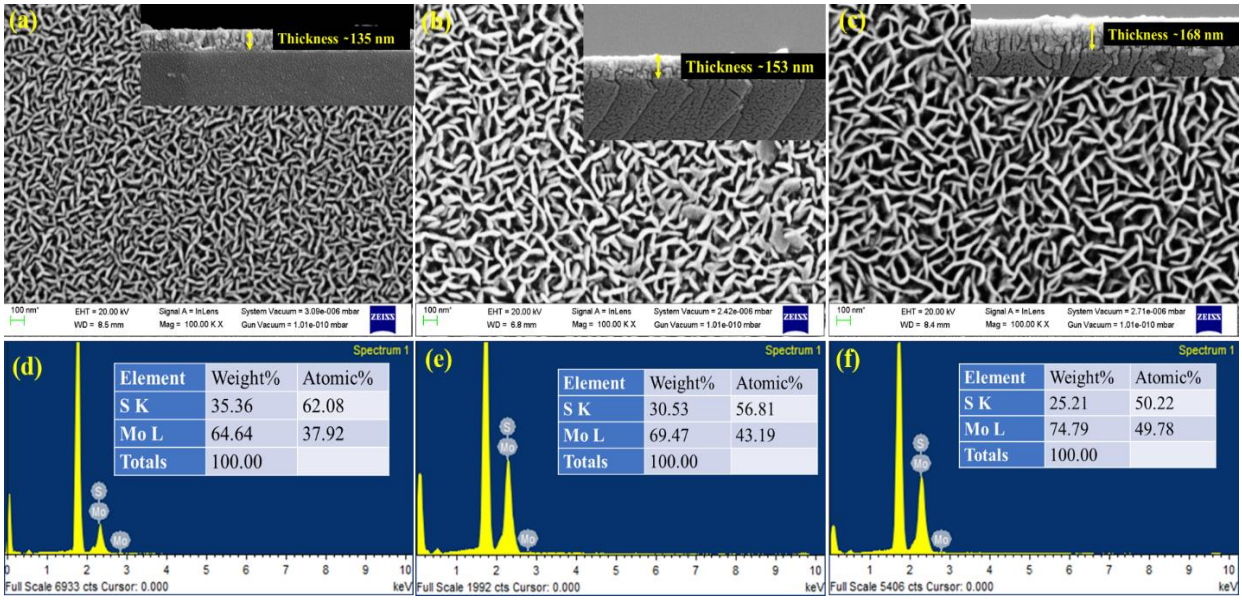

Figure 12. FE-SEM images along with their respective cross sections (insets) of MoS_2 thin films. EDS spectra of MoS_2 films [with the copyright permission of reference (Tyagi et al., 2021)].

Thus, elemental composition can be obtained using EDS. For instance, Tyagi et al. (2021) deposited MoS_2 thin films with various thicknesses. The synthesized MoS_2 thin films having nano worms type morphology were evenly and compactly grown on the glass substrates, as shown in FE-SEM images (Figure 12 (a-c)). They were also measured EDS spectra of all the samples, which are depicted in Figure 12 (d)-(f). They observed the homogeneous distribution of the constituent elements (Mo and S). The EDX spectra of all the samples exposed that Mo and S exist in their desirable ratio.

2.5 Transmission Electron Microscopy

In a transmission electron microscope (TEM), an electron beam is passed through an ultra-thin specimen, which then interacts with the specimen and creates an image on a detector (Inkson, 2016). This image can be magnified and focused to get the desired results.

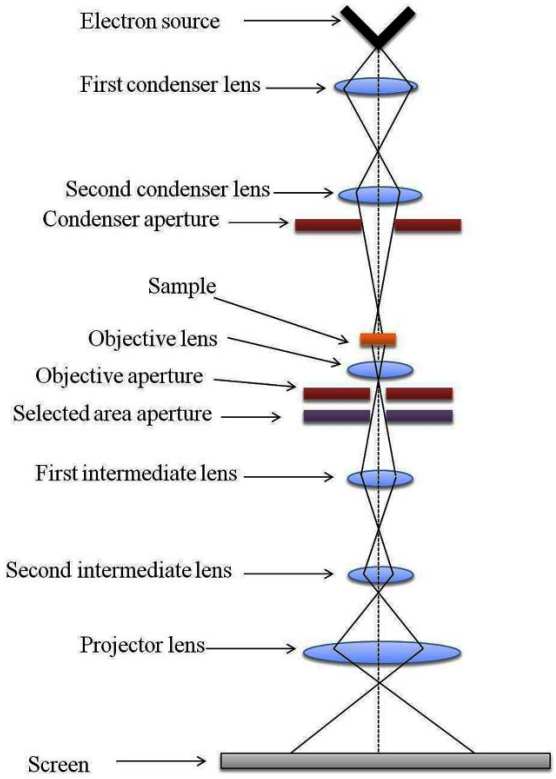

Figure 13. Schematic representation of a transmission electron microscope.

Figure 13 depicts the schematic of a TEM, which is similar to a FE-SEM in many ways. A TEM can be functioned in an image mode and a diffraction mode (Goodhew et al., 2001). In the image mode, the microstructure e.g. the grain size and morphology are studied, while, the diffraction pattern of a sample is studied in the diffraction mode. In TEM, the electron gun (LaB_6) is first situated at the top of the vertical column microscope. The electrons produced through selected potential difference ranging from 4-200 kV. A high resolution of 0.2 nm can be obtained. The electron beam then passes through condenser lenses which demagnify it and help in controlling the area of the specimen to be illuminated. The condenser system controls the brightness and the area of the sample which is sampled by the beam as well as the diffraction pattern. Modern TEMs are fitted with two-condenser illumination system. The first condenser lens sets the demagnification of the gun-crossover. The second lens regulates the convergence angle of the beam leaving

the condenser assembly (Goodhew et al., 2001). The condenser aperture helps in controlling the convergence angle of the beam and its size affects the image quality and intensity of the electron beam. The sample is then placed inside a specimen chamber which is a very delicate part, as a very small sized sample must be placed inside, which should be able to move in the horizontal and vertical directions and tilted by large angles. A side entry specimen holder is used to minimize these difficulties and which holds a 3 mm diameter sample inside the pole pieces of the objective lens. The specimen rod enters the column via an airlock and can be moved by 2-3 mm in the *x* and *y* directions to locate the region of interest and by few mm in the *z*-direction in order to bring the specimen in the object plane of the objective lens. The work of the objective lens is to create initial intermediate image and diffraction pattern, one among them then magnified via the projector lenses and showed on the display (Franken et al., 2020). In Figure 14 schematic diagram for image and diffraction mode in a TEM shows the optics of an objective lens. The first intermediate lens can be changed between two sets as shown in Figure 14. The lens is centered on the image plane of the objective in the image mode. Then, the image is enlarged by the second intermediate lens and passed to the projector lens for display.

Two imaging modes can be used: *bright field* image and *dark field* image (Goodhew et al., 2001). When an incident electron beam interacts with the thin sample, some of the electrons may pass directly through the sample and may undergo elastic or inelastic scattering within the sample. If an aperture is now situated in the back focal plane of the objective lens, it will interrupt all the scattered electrons at an angle larger than certain limit and produce a bright background in the nonexistence of specimen. This is designated as bright field imaging. The thicker region of specimen produces a dark region in the image. Thus, in bright field imaging all the diffracted electrons are stopped by the objective aperture and only undeflected electrons utilized for the image (Mourdikoudis et al., 2018).

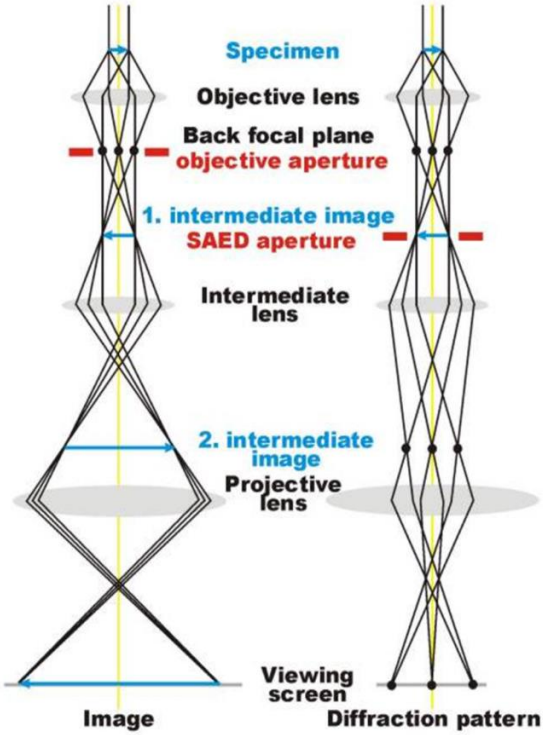

Figure 14. Schematic diagram for image and diffraction mode in a TEM.

However, if the objective aperture is shifted, it can choose a specific diffracted beam and a dark image will appear in the non-existence of specimen. This is designated as dark field imaging. In the diffraction mode of transmission electron microscopy, the intermediate lens is centered on the back focal plane of the objective lens (Reimer, 1997). Subsequently, diffraction pattern is reflected on the screen. Diffraction pattern can be magnified by adjusting the projector lenses. The magnification is described in terms of effective camera length of the system. Diffraction spots are found for single crystals while for polycrystalline specimen's concentric rings are seen in the diffraction pattern.

2.6 Superconducting Quantum Interference Device Magnetometer

A superconducting quantum interference device (SQUID) magnetometer is based on the principle of Josephson effect proposed by the great scientist B. D. Josephson in 1962 (McElfresh, 1994; Macintyre, 1999; Fagaly, 2006; Johnson et al., 2012; Tanaka et al., 2012). He observed that a superconducting current could flow when two superconductors (e.g. Niobium) are separated by a very small insulating gap (e.g. aluminum oxide) named as Josephson junction. Once the junction achieved very low temperature less than 4.2 K, the superconductor current will flow with zero volts through the junction. The magnitude of this current (I_C) flowing through the Josephson junction is a periodic function of the magnetic flux exist in the vicinity of the junction (Macintyre, 1999). The relation between the current I_C as a function of flux ϕ is given by the Equation (6),

$$I_c(\phi) \propto I_c(0) \left|\cos\frac{\pi\phi}{\phi_0}\right| \tag{6}$$

Here, ϕ_0 is one flux quantum. The extreme value of the current therefore occurs for $\phi = n\phi_0$, while minimum value occurs for $\phi = (n+\frac{1}{2})\,\phi_0$. The phenomenon is called as DC Josephson effect which forms the basis for the working of a SQUID magnetometer.

The schematic for the magnetometer is shown in Figure 15 (Fagaly, 2006). The MPMS system possess a superconducting magnet to produce magnetic fields, inductively coupled superconducting detection coil with the sample, a SQUID magnetometer attached to the detection coil and superconducting magnetic shield neighboring the SQUID. A SQUID is the highly delicate instrument to measure the magnetic field, however, it can't directly measure the magnetic field from the sample. The sample is moved through a pair of superconducting detection coils which are fixed to the SQUID sensor using superconducting wires. The current from the detection coils is inductively coupled to the SQUID sensor via these wires. The electronic circuitry used in the SQUID generates an output voltage, which is proportional to the electric current passing through the input coils of SQUID. The SQUID therefore works as current-to-voltage converter, situated around 11 cm beneath the magnet, inside a superconducting shield (Fagaly, 2006; McElfresh, 1994). The magnetic moment is estimated by moving the sample between the detection coils located in the central portion of the magnet and outside the sample chamber. The movement of the sample between the detection coils induces a magnetic moment in the specimen; the change in this magnetic moment produces a current in the detection coils. Since the detection coils, the input coils, and the concerning wires of the SQUID sensor makes a close superconducting loop, any variation in the magnetic flux in the detection coils yields a proportional current in the detection circuit. The change in the amount of current in the detection coils is then transformed to a voltage signal by the SQUID and this output voltage of SQUID is proportional to the magnetic moment of the sample. In a well calibrated system, these voltage changes in the SQUID detector gives extremely accurate values of the specimen's magnetic moment (Buchner et al., 2018).

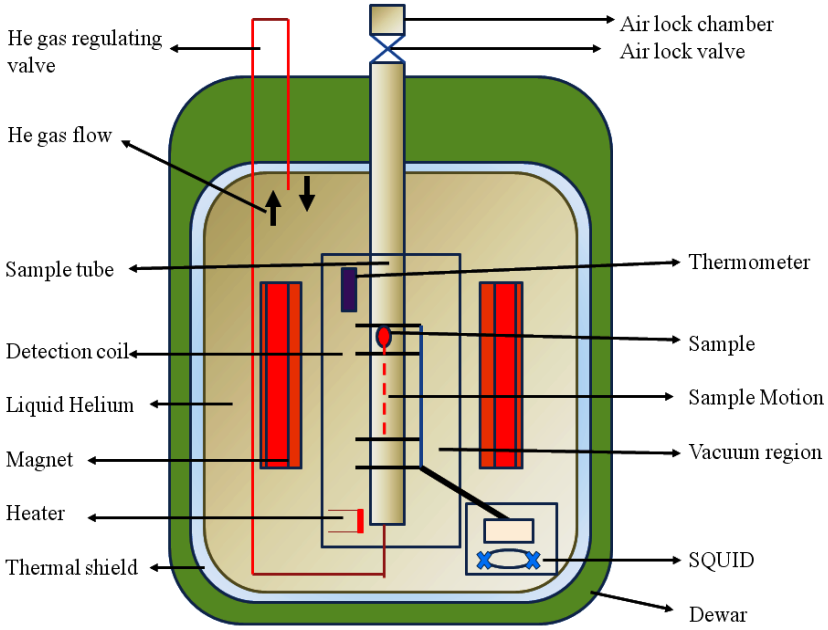

Figure 15. Schematic diagram of the MPMS SQUID magnetometer.

Superconducting detection coil: The detection coil is a second order gradiometer made by winding a single superconducting wire into a set of three coils configuration as depicted in Figure 16. In this arrangement, the upper and lower coils are single turns of the wire which are coiled clockwise while the middle coil consist of two turns wound anticlockwise (Fagaly, 2006; McElfresh, 1994). The coils are put inside the superconducting magnet and outside the sample chamber. This configuration minimizes the noise in the detection circuit which is resulted by the variations in the large magnetic field created by the superconducting magnet. In an ideal case, when the background magnetic field is reducing consistently, the variation in the magnetic flux of the middle two-turn counter-wound coil is cancelled by the variation in the magnetic flux of the upper and lower single turn coils. However, the magnetic moment of the specimen can be estimated since the two-turn counter-wound coil calculate the local variation in the magnetic flux density generated by dipole field of the specimen.

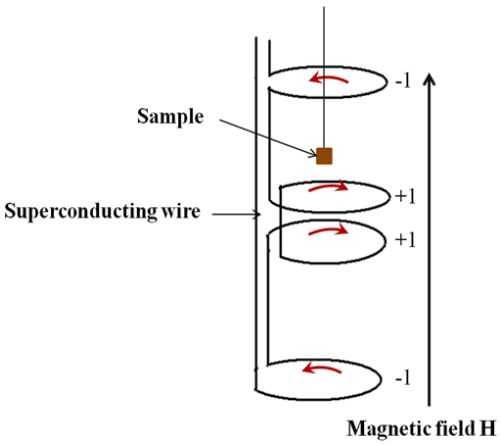

Figure 16. Schematic diagram for the detection coils wound in a second-order gradiometer configuration.

Superconducting magnet: The superconducting magnet is wound in the form a solenoid and forms a closed loop. The magnet can be charged up-to a particular current operating in a persistent mode during a measurement without advantage of any external power supply or current. To modify the current passing through the magnet, the superconducting loop must be opened electrically; this is done by covering a small section of the magnet's superconducting wire with a heater. The small segment of the wire can then be set into a normal (non-superconducting) state by heating, thus making the loop electrically open. By attaching a power supply to the heater, the current in the magnet can now be changed to the desired value thus changing the magnetic field of the magnet. The heater can be now switched off by disconnecting the power supply. The current set in the superconducting wire thus continues to flow, as the wire attains its superconducting state again, sustain the projected value of magnetic field. This situation of magnet state is called persistent mode (McElfresh, 1994; Fagaly, 2006).

Sample space: The sample space is prepared with a tube having inner diameter of 9 mm, kept at low pressure by static, helium gas. There is an airlock valve at the top of the sample space that can be evacuated and purged using the highly pure helium gas. A ball valve situated in between the airlock and the sample space, when opened, makes the airlock and sample space a continuous part. A high thermal uniformity is provided by lining the bottom of the sample space (about 30 cm) with copper. Two thermometers are used to provide and control the sample temperature (McElfresh, 1994; Fagaly, 2006).

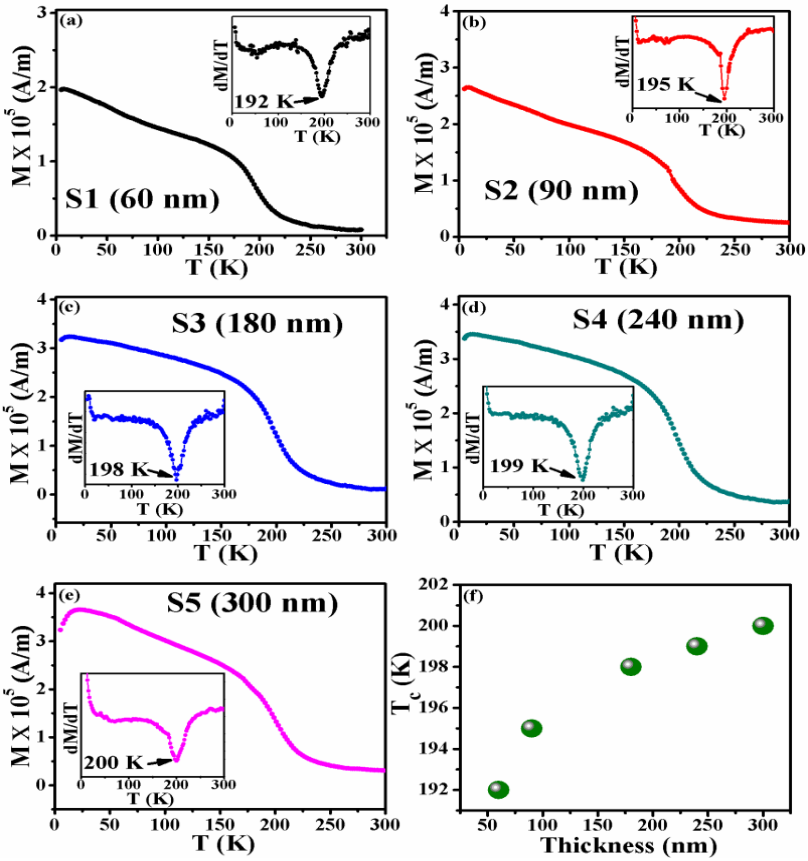

Figure 17. (a-e) M-T curves of samples in the presence of 1 Tesla (T) magnetic field. Insets show the derivative dM/dT versus T curve for all the samples, (f) Variation of Curie temperature (T_C) as a function of thickness [with the copyright permission of Ref. (Singh et al., 2017b)].

The magnetic properties of thin films can be easily measured using SQUID magnetometer (Janů and Soukup, 2017). For instance, the magnetic properties of NNMO thin films (S1-S5) were measured by Singh et al. (2017b) using a SQUID magnetometer. Generally, two types of magnetic measurements can performed using SQUID magnetometer i.e. temperature dependent magnetization (*M-T*) measurements and field dependent magnetization (*M-H*) measurements (Chauhan et al., 2016; Singh et al., 2016; Kumar et al., 2017; Singh and Chandra, 2022). They performed the *M-T* measurements in the temperature ranging from 5 to 300 K with a magnetic field of 1 Tesla. *M-T* curves are shown in Figure 17 (a-e). They also obtained the Curie temperature (T_C) of NNMO films (S1-S5) by calculating the derivative of *M-T* curve with respect to temperature (dM/dT) (insets of Figure 17 (a-e)). T_C is the temperature at which dM/dT curve exhibits the minimum value. They obtained that T_C values increase with film thickness (Figure 17 (f)).

Furthermore, Singh et al. (2017b) also performed *M-H* measurements at 5 K for samples S1-S5, which is shown in Figure 18 (a-e). A clear hysteresis curve reveals the ferromagnetic character of the samples. Dependence of saturation magnetization (determined from the *M-H* curves) on the film thickness is shown in Figure 18 (f). They observed that the value of saturation magnetization increases with film thickness.

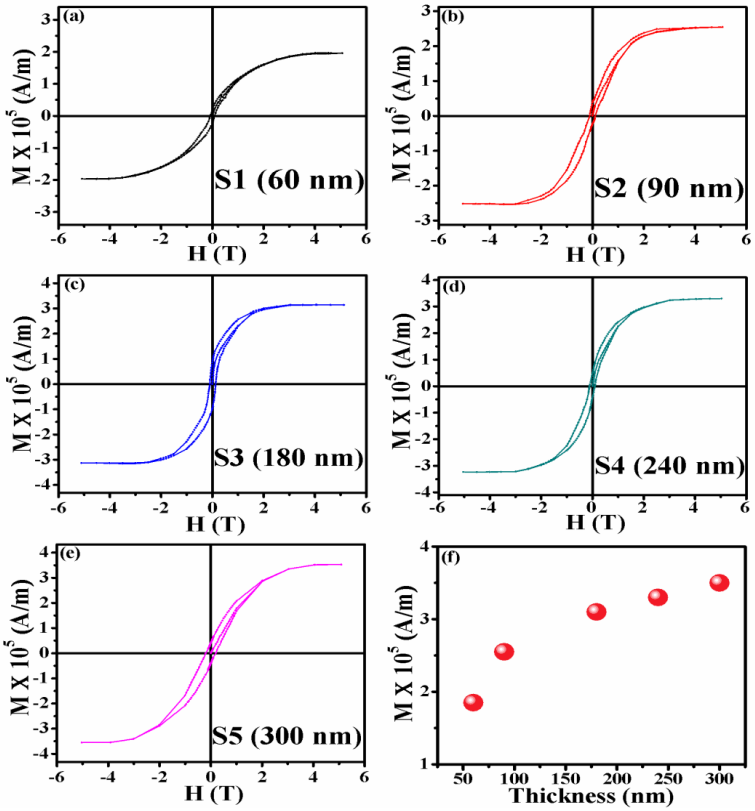

Figure 18. (a-e) M-H curves performed at 5 K for NNMO films, (f) saturation magnetization (M_S) as a function of film thickness [with the copyright permission of Ref. (Singh et al., 2017b)].

2.7 Raman Spectroscopy

In 1924, Dr. C. V. Raman had discovered the fact that when a radiation of light is made incident on a chemical molecule, a segment of the incident light is scattered by the molecule, the wavelength of which differs from that of the incident light (Smith and Dent, 2005; Adar, 2014).

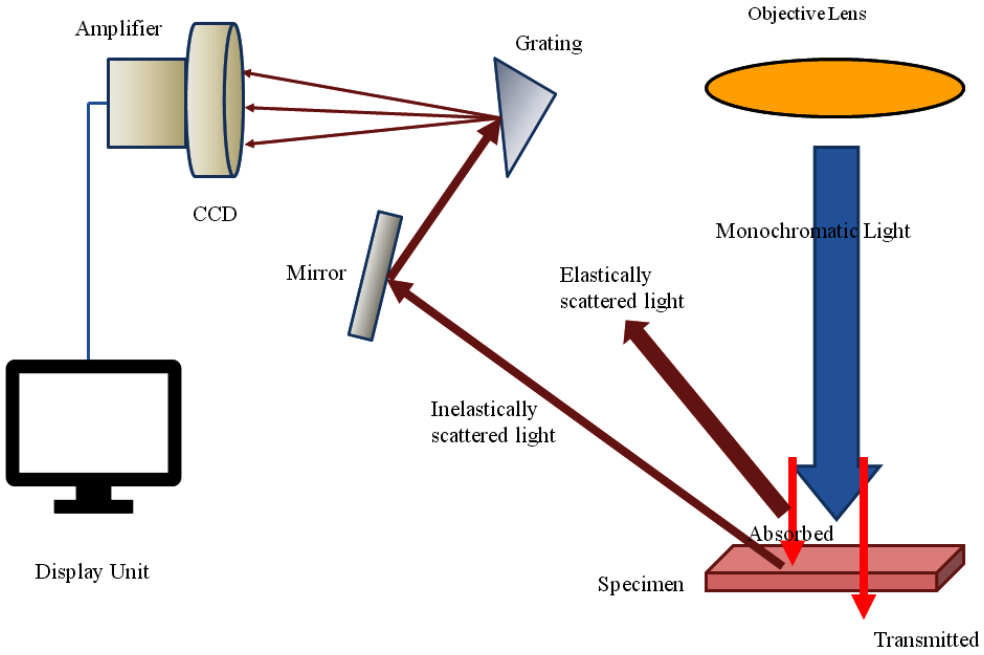

Figure 19. Schematic diagram of a Raman Spectroscopy set-up.

The shift in the λ rely on the chemical structure and bonding of the scattering molecule. The phenomenon results from the similar kind of quantized vibrational variations which are linked with infrared absorption. Thus, the Raman and infra-red absorption spectrum quite closely resemble one another. The advantage of Raman spectroscopy over infra-red absorption is because water molecules does not cause any interference in Raman spectra and can be easily attained even for aqueous solutions. Glass and quartz cells can be used instead of sodium chloride or other atmospherically unstable window materials (Smith and Dent, 2005; Bahlawane, 2010).

The schematic diagram for a Raman scattering set-up is shown in Figure 19. The Raman spectra can be obtained by bringing a specimen in the path of a powerful laser source or near infra-red monochromatic radiation (Rostron et al., 2016; Orlando et al., 2021). A spectrometer placed at some angle with the sample can collect the scattered radiation in a range of angles. The emitted radiation spectrum is of three types: *Stokes, Anti-stokes and Rayleigh scattering* (Figure 20). In Raman scattering, the incident light falls on the molecule and polarizes the electron region in the surrounding of nuclei thereby exciting the electrons to a short-lived virtual state. At room temperature, a large number of molecules are in their minimum energy states. When the scattering occurs by electron cloud distortion, the photons are scattered with very small change in their frequency. Such kind of scattering process occurs due to elastic scattering and is most dominant in most of the compounds (Zhang et al., 2016; Xu et al., 2018). This scattering is known as Rayleigh scattering.

However, when the scattering creates a nuclear motion, either incident photon transfers energy to the molecule (Stokes) or the molecule gives some energy to the scattered photon (Anti-stokes). This scattering is inelastic and the energy of the scattered photon will differ by the energy of the scattered photon by one vibrational unit. This is known as Raman scattering. The x-axis on a Raman spectrum is shift in wavenumber Δν corresponds to the difference in wavenumber of incident (source) and scattered (out coming) radiation (Smith and Dent, 2005).

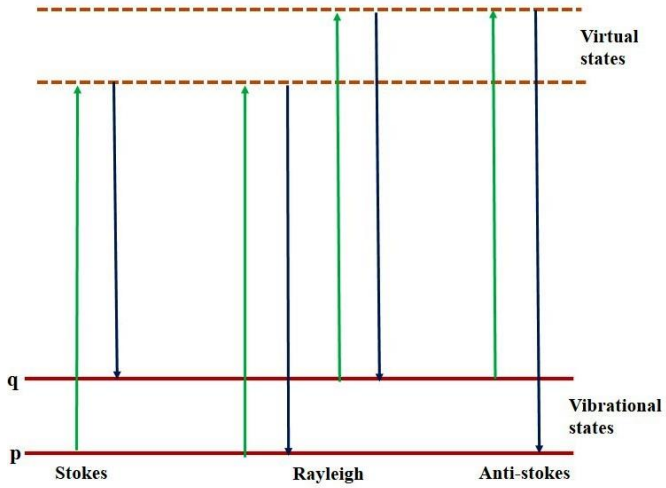

Figure 20. Diagram for Rayleigh and Raman scattering processes.

Raman spectra is a vital tool to identify the strain in the thin films (Zhang et al., 2016; Xu et al., 2018; Orlando et al., 2021). In this regard, Raman spectra have been taken from the ref. (Singh et al., 2017b), which is shown in Figure 21. They found the similar spectra for all the samples and concluded that the samples possess same composition. They observed the antisymmetric stretching (AS) and symmetric stretching (S) peaks for the NNMO thin films at a lower frequency than the corresponding peaks in bulk NNMO. They conveyed that a clear red shift (shift towards lower frequency) of the Raman peaks as compared to bulk sample confirm the tensile strain state of thin film.

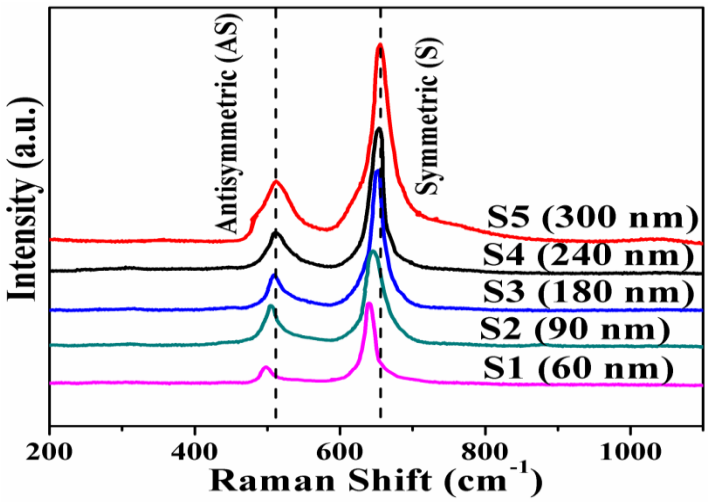

Figure 21. Raman spectra of NNMO thin films for various thickness [with the copyright permission of Reference (Singh et al., 2017b)].

2.8 X-ray Absorption Spectroscopy (XAS)

X-ray absorption spectroscopy (XAS) in the soft X-ray energy range is an effective tool used for material characterization in the different fields of basic science and engineering (Lim et al., 2022; Singh et al., 2022a;

Lim and Song, 2024). This is an element selective techniques and provides material characteristics for specific element held at specific absorption edges, chemical species characteristics (π*, σ*), anisotropy of molecular species by mean of estimating lattice anisotropy and molecular orientation using linearly polarized X-rays while uses circularly polarized X-rays for probing magnetic material (Http://Www.Rrcat.Gov.in/Technology/Accel/Srul/Beamlines/Mcd_pes.Html, n.d.). It is a very common technique that is used to decide the electronic structure of material. Generally, the measurement is carried out at synchrotron radiation sources that deliver tunable and strong X-ray beams. Specimen can be in the solid state, liquid and gaseous phase. A crystalline monochromator is used to tune the photon energy and records the XAS data where core electrons can be excited in the photon energy ranging from 0.1 to 100 keV (Singh et al., 2022b). Figure 22 depicts the schematic diagram of polarized soft XAS beamline.

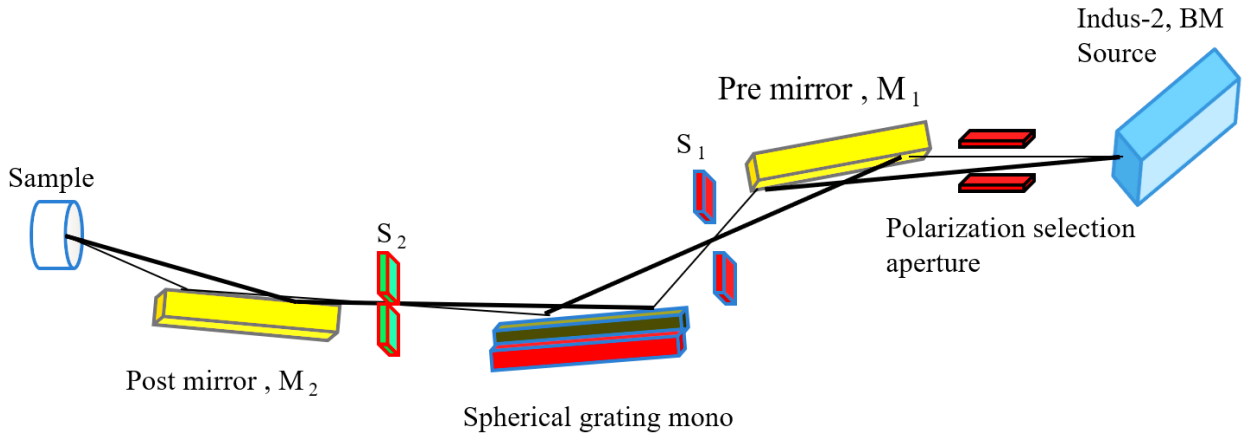

Figure 22. Schematic diagram for soft X-ray absorption spectroscopy.

Polarized soft XAS beamline placed at the bending magnet of synchrotron source works in the energy ranging from 100 to 1200 eV and yields the necessity of selection of X-ray absorption measurements. The edge name can be decided on the basis of the excited electron: the principal quantum numbers n = 1, 2, and 3, represent the K, L, and M edges, respectively. For example, the K-edge involves excitation of 1s electron, whereas L-edge corresponds to the excitation of a 2s or 2p electron (Figure 23) ("Https://En.Wikipedia.Org/Wiki/X-Ray_absorption_spectroscopy," n.d.). The absorption threshold can be achieved by the decay to the lowermost vacant levels: (a) the levels at the Fermi energy in conductors providing a "rising edge"; (b) the bound core excitons in insulators with a Lorentzian line-shape (Https://En.Wikipedia.Org/Wiki/X-Ray_absorption_spectroscopy, n.d.).

XAS belongs to the one of the categories of absorption spectroscopy involves a core initial state. In this regard, the selection rules choose the symmetry of the final states in a range mixture of number of constituents. The dipole allowed transitions (i.e. $\Delta\ell = \pm 1$) to vacant final levels are responsible for the observation of strongest features. For instance, the strongest features of a K-edge are mainly because of the core transitions occurs from the 1s to 2p states and the L_3 edge are owing to transitions from 2p to 3d states. XAS measurement can be distributed into three classes which can provide complementary outputs to each other are metal K-edge, metal L-edge and ligand K-edge, respectively (Https://En.Wikipedia.Org/Wiki/X-Ray_absorption_spectroscopy, n.d.).

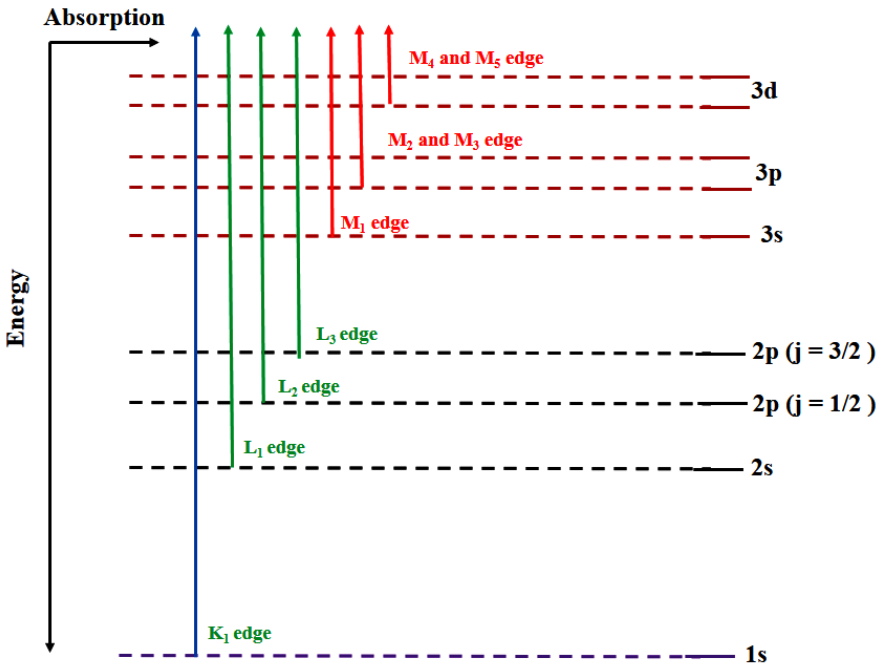

Figure 23. Diagram for transitions that contribute to XAS edges.

In a study Singh et al. (2018), the Mn *2p* edge XAS spectra of $Nd_{2-x}Sr_xMnNiO_6$ (where, x = 0 to 1) polycrystalline samples were measured, as shown in Figure 24. The nature of spectra was similar to that of an Mn^{4+} system, for all the Sr compositions (Sánchez et al., 2002). For comparison, they were also measured the spectra of $LaMnO_3$ in which Mn belongs to 3+ state. Thus, though the formal valency of Mn remains fixed (4+) for all the samples, however, small changes occur in the absorption intensity with Sr doping.

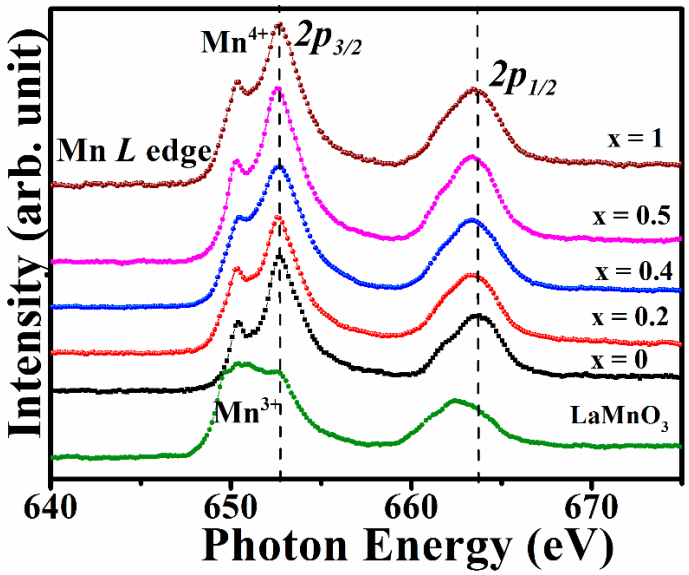

Figure 24. Mn 2p XAS spectra of $Nd_{2-x}Sr_xMnNiO_6$ (x = 0 to 1). Reference spectra of $LaMnO_3$ (Mn^{3+}) is shown [with the copyright permission of Reference (Singh et al., 2018)].

2.9 X-Ray Photoelectron Spectroscopy (XPS)

X-ray Photoelectron Spectroscopy (XPS) is a commonly used surface analysis technique that provides valuable insights into the surface chemistry of a wide range of materials, including metals, semiconductors, polymers, ceramics, and thin films (Islam et al., 2020; Greczynski and Hultman, 2020; Greczynski and Hultman, 2022; Sancho-Albero et al., 2023). Basically, it is a non-destructive analytical technique which is mainly used to analysis the elemental composition, chemical bonding, and electronic state of a material's surface. The schematic representation of XPS setup has been shown in the Figure 25.

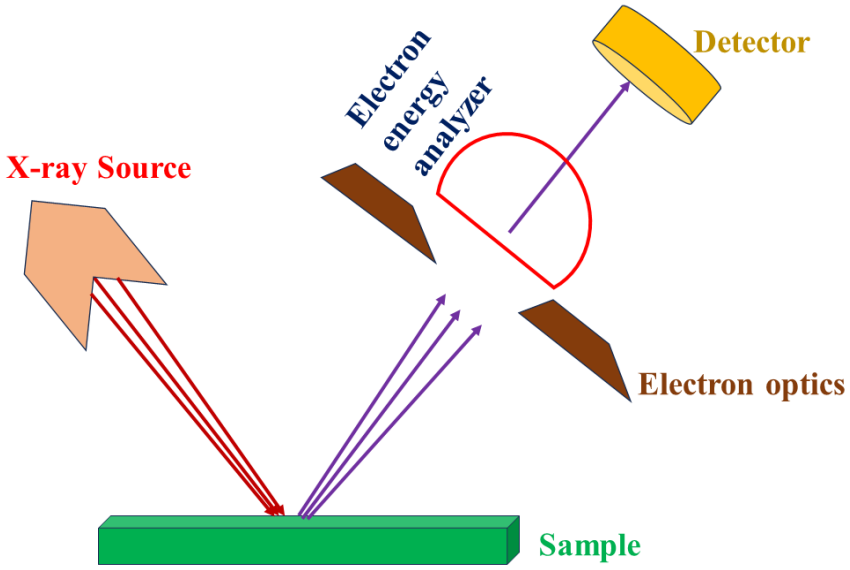

Figure 25. Schematic representation of XPS setup.

In XPS, a high-energy X-ray source has been used which emits X-ray photons with a specific energy (Greczynski and Hultman, 2020). The energy of the X-ray photons is chosen to exceed the binding energy of the electrons in the sample. When the X-ray photons strike the surface of the sample, they can interact with the electrons present in the outermost layers of atoms. This interaction is responsible for the emission of photoelectrons from the sample. The kinetic energy of the emitted electrons is comparable to the difference between the two energies: one is the binding energy of the electron in the atom and the second one is the energy of the incident X-ray photon (Sancho-Albero et al., 2023). A hemispherical electron energy analyzer has been employed to collect and analyze the emitted photoelectrons. Photoelectrons can be separated based on their kinetic energy, by using the analyzer which consists of a series of electric and magnetic fields. The analyzer can sequentially determine the kinetic energy of the emitted electrons by changing the electric field strength, allowing for the calculation of their binding energies. The energy of the emitted electrons corresponds to the specific elements present in the sample, as each element has its own characteristics features of binding energies. The elemental composition of the surface can be recognized by comparing the calculated binding energies to known reference spectra (Greczynski and Hultman, 2022). Moreover, the intensity of the emitted photoelectrons yields information about the relative abundance of each element. XPS also provides valuable insights into the chemical bonding and electronic state of the surface atoms. The oxidation state of the elements can be determined by analyzing the shape and position of the XPS peaks (Balasubramanian et al., 2018). Chemical shifts in the binding energy suggests the presence of different chemical species or chemical interactions within the sample.

Thus, the above discussed characterization facilities are helpful to investigate the various properties of magnetic thin films. Based on the previous studies, we have also summarized each characterization technique and its uses in Table 1.

Table 1. Summary of literature on magnetic thin film characterization.

Reference	Tools Used	Summary of Results/Findings
Singh et al. (2018)	X-ray Absorption Spectroscopy (XAS)	Investigated Mn 2p edge XAS spectra of $Nd_{2-x}Sr_xMnNiO_6$ polycrystalline samples. Found similarities with Mn^{4+} system.
Singh et al. (2017c)	Superconducting Quantum Interference Device (SQUID)	Measured magnetic properties of NNMO thin films (S1-S5) using SQUID magnetometer. Found clear hysteresis curve indicating ferromagnetism.
Tyagi et al. (2021)	Field Emission Scanning Electron Microscopy (FE-SEM)	Examined morphology of MoS_2 thin films with various thicknesses using FE-SEM. Observed nanoworms type morphology.
Singh and Chandra (2018)	X-ray Reflectivity (XRR)	Deposited LNMO, LMO, and [LNMO/LMO]15 multilayers on $LaAlO_3$ substrate and studied their XRR patterns.
Smith and Dent (2005), Adar (2014)	Raman Spectroscopy	Used Raman spectroscopy to identify strain in thin films. Found clear red shift in Raman peaks indicating tensile strain.
Goodhew et al. (2001)	Transmission Electron Microscopy (TEM)	Used TEM to study microstructure and morphology of materials.
Fagaly (2006), Johnson et al. (2012), Tanaka et al. (2012)	Superconducting Quantum Interference Device (SQUID) Magnetometer	Utilized SQUID magnetometer to measure magnetic properties of materials.
https://en.wikipedia.org/wiki/X-Ray_absorption_spectroscopy	X-ray Absorption Spectroscopy (XAS)	Reviewed the principles and applications of XAS in material characterization, focusing on core initial state and selection rules.
Singh et al. (2017c)	Field Emission Scanning Electron Microscopy (FE-SEM), X-ray Diffraction (XRD)	Analyzed surface morphological properties and crystallographic structure of thin films using FE-SEM and XRD.
Sánchez et al. (2002)	X-ray Absorption Spectroscopy (XAS)	Investigated Mn 2p edge XAS spectra of doped polycrystalline samples. Found spectral similarities with Mn^{4+} system.
Adar (2014)	Raman Spectroscopy	Studied strain in thin films using Raman spectroscopy. Observed red shift in Raman peaks indicative of tensile strain.
Macintyre (1999)	Superconducting Quantum Interference Device (SQUID)	Reviewed the operating principle and applications of SQUID magnetometers in measuring magnetic properties of materials.
Tyagi et al. (2021)	Energy dispersive spectrometer (EDS)	homogeneous distribution of the constituent elements (Mo and S) in desirable ratio
Balasubramanian et al. (2018)	X-ray photoelectron spectroscopy (XPS)	Mn and Ni are in 4+ and 2+ states respectively

3. Conclusion

In summary, the role of various techniques in characterizing the magnetic thin films has been described in the present review. In this regard, some important characterization tools such as X-Ray Diffraction, X-Ray reflectivity, Field emission scanning electron microscopy, Energy dispersive spectrometer, Transmission electron microscopy, Superconducting quantum interference device, Raman spectroscopy and X-ray absorption spectroscopy are discussed. The basic principle, construction and working of these techniques have been explained in detail. Some experimental results obtained using these techniques are also discussed in the present article. The characterization of nano materials via progressive techniques provides the information of structural, physical, chemical, thermal, and magnetic etc. properties of these materials. The better understanding of the properties of nanostructured material is helpful in the development of nanostructured based devices.

Through this review article, we described the uses of several magnetic thin film's characterization methods, highlighting on their advantages, as well as on mentioning how they can be successfully combined and how they can complement each other. The use of several characterization techniques is required for determining well and completely even a single property of thin films, since the variety of features are associated with the thin films. By explaining the functioning of each technique in a systematic way, our review will serve as a powerful guide to the scientific community. This way will help the researchers to choose the most appropriate techniques for the characterization of their samples. It will also provide the potential to judge the use of these techniques in a more precise manner.

Obviously, it is a challenging task for the scientific community as several techniques needed further improvements like accuracy and resolution. Hence, we hope that the careful reading of this review will help to recognize which techniques merit efforts for further technical improvements.

Conflict of Interest

The authors declare that they have no known competing financial interests or personal relationships that could have appeared to influence the work reported in this paper.

Acknowledgments

No acknowledgment was reported by the author(s).

References

Adar, F. (2014). Raman spectra of metal oxides. *Spectroscopy*, *29*(10), 14. https://images2.advanstar.com/PixelMags/spectroscopy/pdf/2014-10.pdf.

Ali, A., Chiang, Y.W., & Santos, R.M. (2022). X-ray diffraction techniques for mineral characterization: A review for engineers of the fundamentals, applications, and research directions. *Minerals*, *12*(2), 205. https://doi.org/10.3390/min12020205.

Ali, A., Zhang, N., & Santos, R.M. (2023). Mineral characterization using scanning electron microscopy (sem): a review of the fundamentals, advancements, and research directions. *Applied Sciences*, *13*(23), 12600. https://doi.org/10.3390/app132312600.

Ameh, E.S. (2019). A review of basic crystallography and x-ray diffraction applications. *The International Journal of Advanced Manufacturing Technology*, *105*(7), 3289-3302.

Bajaj, K., Jesudasan, J., Bagwe, V., Kothari, D.C., & Raychaudhuri, P. (2007a). Electroresistive effects in electron doped manganite La0. 7Ce0. 3MnO3 thin films. *Journal of Physics: Condensed Matter*, *19*(4), 046208. https://doi.org/10.1088/0953-8984/19/4/046208.

Bajaj, K., Jesudasan, J., Bagwe, V., Kothari, D.C., & Raychaudhuri, P. (2007b). Correlation between effects of electric current and magnetic field on transport properties of electron-doped manganite La0. 7Ce0. 3MnO3 thin films. *Journal of Physics: Condensed Matter*, *19*(38), 382202. https://doi.org/10.1088/0953-8984/19/38/382202.

Balasubramanian, P., Joshi, S.R., Yadav, R., de Groot, F.M., Singh, A.K., Ray, A., Tulika, M., & Malik, V. (2018). Electronic structure of Pr2MnNiO6 from x-ray photoemission, absorption and density functional theory. *Journal of Physics: Condensed Matter*, *30*(43), 435603.

Buchner, M., Höfler, K., Henne, B., Ney, V., & Ney, A. (2018). Tutorial: Basic principles, limits of detection, and pitfalls of highly sensitive SQUID magnetometry for nanomagnetism and spintronics. *Journal of Applied Physics*, *124*(16), 161101. https://doi.org/10.1063/1.5045299.

Bunaciu, A.A., UdriȘTioiu, E.G., & Aboul-Enein, H.Y. (2015). X-ray diffraction: instrumentation and applications. *Critical Reviews in Analytical Chemistry*, *45*(4), 289-299. https://doi.org/10.1080/10408347.2014.949616.

Chauhan, S., Singh, A.K., Srivastava, S.K., & Chandra, R. (2016). Study of magnetic behavior in hexagonal-YMn1−xFexO3 (x= 0 and 0.2) nanoparticles using remanent magnetization curves. *Journal of Magnetism and Magnetic Materials*, *414*, 187-193. https://doi.org/10.1016/j.jmmm.2016.04.074.

Cui, B., Song, C., Wang, G.Y., Mao, H.J., Zeng, F., & Pan, F. (2013). Strain engineering induced interfacial self-assembly and intrinsic exchange bias in a manganite perovskite film. *Scientific Reports*, *3*(1), 2542. https://doi.org/10.1038/srep02542.

Cullity, B.D. (1956). *Elements of X-ray diffraction*. Addison-Wesley Publishing.

Delvallée, A., Feltin, N., Ducourtieux, S., Trabelsi, M., & Hochepied, J.F. (2015). Direct comparison of AFM and SEM measurements on the same set of nanoparticles. *Measurement Science and Technology*, *26*(8), 085601. https://doi.org/10.1088/0957-0233/26/8/085601.

Fagaly, R.L. (2006). Superconducting quantum interference device instruments and applications. *Review of Scientific Instruments*, *77*(10), 101101. https://doi.org/10.1063/1.2354545.

Franken, L.E., Grünewald, K., Boekema, E.J., & Stuart, M.C. (2020). A technical introduction to transmission electron microscopy for soft-matter: Imaging, possibilities, choices, and technical developments. *Small*, *16*(14), 1906198. https://doi.org/10.1002/smll.201906198.

Gajek, M., Bibes, M., Barthélémy, A., Bouzehouane, K., Fusil, S., Varela, M., Fontcuberta, & Fert, A. (2005). Spin filtering through ferromagnetic Bi Mn O 3 tunnel barriers. *Physical Review B*, *72*(2), 020406. https://doi.org/10.1103/PhysRevB.72.020406.

Ghimpu, L., Tiginyanu, I., Lupan, O., Mishra, Y.K., Paulowicz, I., Gedamu, D., Cojocaru, A., & Adelung, R. (2013). Effect of Al Sn—Doping on properties of zinc oxide nanostructured films grown by magnetron sputtering. In *CAS 2013 International Semiconductor Conference* (Vol. 1, pp. 133-136). IEEE. Sinaia, Romania.

Goldstein, A., Soroka, Y., Frušić-Zlotkin, M., Popov, I., & Kohen, R. (2014). High resolution SEM imaging of gold nanoparticles in cells and tissues. *Journal of Microscopy*, *256*(3), 237-247.

Goodhew, P.J., & Humphreys, J. (2000). *Electron microscopy and analysis*. CRC press, London.

Greczynski, G., & Hultman, L. (2020). X-ray photoelectron spectroscopy: towards reliable binding energy referencing. *Progress in Materials Science*, *107*, 100591. https://doi.org/10.1016/j.pmatsci.2019.100591.

Greczynski, G., & Hultman, L. (2022). A step-by-step guide to perform x-ray photoelectron spectroscopy. *Journal of Applied Physics*, *132*(1), 011101. https://doi.org/10.1063/5.0086359.

Http://www.Rrcat.Gov.in/Technology/Accel/Srul/Beamlines/Mcd_pes.Html. n.d.

Https://En.Wikipedia.Org/Wiki/X-Ray_absorption_spectroscopy. n.d.

Husain, S., Kumar, A., Akansel, S., Svedlindh, P., & Chaudhary, S. (2017). Anomalous Hall effect in ion-beam sputtered Co2FeAl full Heusler alloy thin films. *Journal of Magnetism and Magnetic Materials*, *442*, 288-294.

Inkson, B.J. (2016). Scanning electron microscopy (SEM) and transmission electron microscopy (TEM) for materials characterization. In *Materials Characterization using Nondestructive Evaluation (NDE) Methods* (pp. 17-43). Woodhead publishing. https://doi.org/10.1016/B978-0-08-100040-3.00002-X.

Islam, K., Sultana, R., Rakshit, A., Goutam, U.K., & Chakraborty, S. (2020). X-ray reflectivity and X-ray photoelectron spectroscopy studies on reactively sputtered Nb 2 O 5-based thin-film devices. *SN Applied Sciences*, *2*(4), 782. https://doi.org/10.1007/s42452-020-2558-x.

Janů, Z., & Soukup, F. (2017). Continuous reading SQUID magnetometer and its applications. *Review of Scientific Instruments*, *88*(6), 065104. https://doi.org/10.1063/1.4984943.

Johnson, C., Adolphi, N.L., Butler, K.L., Lovato, D.M., Larson, R., Schwindt, P.D., & Flynn, E.R. (2012). Magnetic relaxometry with an atomic magnetometer and SQUID sensors on targeted cancer cells. *Journal of Magnetism and Magnetic Materials*, *324*(17), 2613-2619. https://doi.org/10.1016/j.jmmm.2012.03.015.

Kamerbeek, A.M., De Vries, E.K., Dankert, A., Dash, S.P., Van Wees, B.J., & Banerjee, T. (2014). Electric field effects on spin accumulation in Nb-doped SrTiO3 using tunable spin injection contacts at room temperature. *Applied Physics Letters*, *104*(21), 212106. https://doi.org/10.1063/1.4880895.

Khan, H., Yerramilli, A.S., D'Oliveira, A., Alford, T.L., Boffito, D.C., & Patience, G.S. (2020). Experimental methods in chemical engineering: X-ray diffraction spectroscopy—XRD. *The Canadian Journal of Chemical Engineering*, *98*(6), 1255-1266. https://doi.org/10.1002/cjce.23747.

Khan, I., Saeed, K., & Khan, I. (2019). Nanoparticles: Properties, applications and toxicities. *Arabian Journal of Chemistry*, *12*(7), 908-931. https://doi.org/10.1016/j.arabjc.2017.05.011.

Kumar, A., Sanger, A., Singh, A.K., Kumar, A., Kumar, M., & Chandra, R. (2017). Experimental evidence of spin glass and exchange bias behavior in sputtered grown α-MnO2 nanorods. *Journal of Magnetism and Magnetic Materials*, *433*, 227-233. https://doi.org/10.1016/j.jmmm.2017.02.061.

Kumar, N., Kim, N.G., Park, Y.A., Hur, N., Jung, J.H., Han, K.J., & Yee, K.J. (2008). Epitaxial growth of terbium iron garnet thin films with out-of-plane axis of magnetization. *Thin Solid Films*, *516*(21), 7753-7757. https://doi.org/10.1016/j.tsf.2008.05.032.

Lim, W.C., & Song, J. (2024). Effect of heating/cooling rate on the local electronic structure of amorphous calcium carbonate. *Prabha Materials Science Letters*, *3*(1), 77-84. https://doi.org/10.33889/pmsl.2024.3.1.005.

Lim, W.C., Singh, J.P., Song, J., Seong, T.Y., & Chae, K.H. (2022). Structural, optical, and magnetic properties of Ag+, Mn+ and Ar+ ions implanted ZnO thin films: Effect of implantation dose and stopping energy. *RSC Advances*, *12*(46), 29666-29676. https://doi.org/10.1039/d2ra05430b.

Low, T., Rodin, A.S., Carvalho, A., Jiang, Y., Wang, H., Xia, F., & Neto, A.C. (2014). Tunable optical properties of multilayer black phosphorus thin films. *Physical Review B*, *90*(7), 075434. https://doi.org/10.1103/PhysRevB.90.075434.

Macintyre, S.A. (1999). *Magnetic field measurement*. CRC Press LLC.

Mazzaglia, A., Scolaro, L.M., Mezzi, A., Kaciulis, S., Caro, T.D., Ingo, G.M., & Padeletti, G. (2009). Supramolecular colloidal systems of gold nanoparticles/amphiphilic cyclodextrin: A FE-SEM and XPS investigation of nanostructures assembled onto solid surface. *The Journal of Physical Chemistry C*, *113*(29), 12772-12777. https://doi.org/10.1021/jp903673x.

McElfresh, M. (1994). Fundamentals of magnetism and magnetic measurements featuring Quantum Design's magnetic property measurement system. *Quantum Design*, *11578*, 132.

Mishra, A., Srivastava, S.K., Kumar, A., Dubey, P., Chauhan, S., Singh, A.K., Kaur, D., & Chandra, R. (2014). Thickness dependent exchange bias in co-sputter deposited Ni–Mn–Al Heusler alloy hard nanostructured thin films. *Thin Solid Films*, *572*, 142-146. https://doi.org/10.1016/j.tsf.2014.08.014.

Mourdikoudis, S., Pallares, R.M., & Thanh, N.T. (2018). Characterization techniques for nanoparticles: comparison and complementarity upon studying nanoparticle properties. *Nanoscale*, *10*(27), 12871-12934. https://doi.org/10.1039/c8nr02278j.

Narayan, R.J. (2005). Nanostructured diamondlike carbon thin films for medical applications. *Materials Science and Engineering: C*, *25*(3), 405-416. https://doi.org/10.1016/j.msec.2005.01.026.

Ohring, M. (1992). *The materials science of thin films academic press*. San Diego, Boston, New York.

Orlando, A., Franceschini, F., Muscas, C., Pidkova, S., Bartoli, M., Rovere, M., & Tagliaferro, A. (2021). A comprehensive review on Raman spectroscopy applications. *Chemosensors*, *9*(9), 262. https://doi.org/10.3390/chemosensors9090262.

Raju, M., Chaudhary, S., & Pandya, D.K. (2013). Multi-jump magnetic switching in ion-beam sputtered amorphous Co20Fe60B20 thin films. *Journal of Applied Physics*, *114*(5), 053911. https://doi.org/10.1063/1.4817653.

Rana, K.G., Parui, S., & Banerjee, T. (2013). Probing electron transport across a LSMO/Nb: STO heterointerface at the nanoscale. *Physical Review B*, *87*(8), 085116. https://doi.org/10.1103/PhysRevB.87.085116.

Reimer, L. (2013). *Transmission electron microscopy: physics of image formation and microanalysis* (Vol. 36). Springer.

Rostron, P., Gaber, S., & Gaber, D. (2016). Raman spectroscopy, review. *International Journal of Engineering and Technical Research*, *6*(1), 50-64

Sánchez, M.C., García, J., Blasco, G., Subías, & Perez-Cacho, J. (2002). Local electronic and geometrical structure of $LaNi_{1-x}Mn_xO_{3+\square}$ perovskites determined by x-ray-absorption spectroscopy. *Physical Review B* 65: 144409. https://doi.org/10.1103/PhysRevB.65.144409.

Sancho-Albero, M., Martín-Pardillos, A., Irusta, S., Sebastián, V., Cebolla, V.L., Pazo-Cid, R., Martín-Duque, P., & Santamaría, J. (2023). X-ray photoelectron spectroscopy (xps) analysis of nitrogen environment in small extracellular vesicle membranes: A potential novel technique with application for cancer screening. *Cancers*, *15*(9), 2479. https://doi.org/10.3390/cancers15092479.

Scimeca, M., Bischetti, S., Lamsira, H.K., Bonfiglio, R., & Bonanno, E. (2018). Energy dispersive X-ray (EDX) microanalysis: A powerful tool in biomedical research and diagnosis. *European Journal of Histochemistry: EJH*, *62*(1), 89-99. https://doi.org/10.4081/ejh.2018.2841.

Singh, A.K., & Chandra, R. (2018). Thickness dependent interfacial magnetic coupling in [La2NiMnO6/LaMnO3] multilayers. *Journal of Magnetism and Magnetic Materials*, *448*, 180-185. https://doi.org/10.1016/j.jmmm.2017.08.080.

Singh, A.K., & Chandra, R. (2022). Spin glass and exchange bias phenomena in NdSrNiMnO6 nanoparticles: Role of antiferromagnetic antisite disorders. *Journal of Magnetism and Magnetic Materials*, *549*, 169048. https://doi.org/10.1016/j.jmmm.2022.169048.

Singh, A.K., Balasubramanian, P., Singh, A., Gupta, M.K., & Chandra, R. (2018). Structural transformation, Griffiths phase and metal-insulator transition in polycrystalline Nd2− xSrxNiMnO6 (x= 0, 0.2, 0.4, 0.5 and 1) compound. *Journal of Physics: Condensed Matter*, *30*(35), 355401.

Singh, A.K., Chauhan, S., & Chandra, R. (2017a). Antisite disorder induced spin glass and exchange bias effect in Nd2NiMnO6 epitaxial thin film. *Applied Physics Letters*, *110*(10), 102402. https://doi.org/10.1063/1.4978354.

Singh, A.K., Chauhan, S., & Chandra, R. (2017b). Thickness dependent structural and magnetic properties of Nd2NiMnO6 epitaxial thin films. *Thin Solid Films*, *625*, 17-23. https://doi.org/10.1016/j.tsf.2017.01.056.

Singh, A.K., Chauhan, S., Balasubramanian, P., Srivastava, S.K., & Chandra, R. (2017c). Influence of substrate induced strain on B-site ordering and magnetic properties of Nd2NiMnO6 epitaxial thin films. *Thin Solid Films*, *629*, 49-54. https://doi.org/10.1016/j.tsf.2017.03.048.

Singh, A.K., Chauhan, S., Srivastava, S.K., & Chandra, R. (2016). Influence of antisite disorders on the magnetic properties of double perovskite Nd2NiMnO6. *Solid State Communications*, *242*, 74-78. https://doi.org/10.1016/j.ssc.2016.04.020.

Singh, A.P., Gandhi, D.D., Moore, R., & Ramanath, G. (2007). Thermal stability of molecularly functionalized mesoporous silica thin films. *Journal of Applied Physics*, *102*(4), 044507. https://doi.org/10.1063/1.2771042.

Singh, J.P., Nandy, S., Chae, K.H., & Lee, S. (2022a). X-ray absorption spectroscopy for estimation of oxidation state, chemical fraction and local atomic structure of materials. *Prabha Materials Science Letters*, *1*(1), 21-29. https://doi.org/10.33889/pmsl.2022.1.1.004.

Singh, J.P., Paidi, A.K., Chae, K.H., Lee, S., & Ahn, D. (2022b). Synchrotron radiation based X-ray techniques for analysis of cathodes in Li rechargeable batteries. *RSC Advances*, *12*(31), 20360-20378.

Smith, E., & Dent, G. (2019). *Modern Raman spectroscopy: A practical approach*. John Wiley & Sons. USA.

Sofin, R.G.S., Arora, S.K., & Shvets, I.V. (2011). Positive antiphase boundary domain wall magnetoresistance in Fe 3 O 4 (110) heteroepitaxial films. *Physical Review B*, *83*(13), 134436. https://doi.org/10.1103/PhysRevB.83.134436.

Tanaka, S., Kitamura, Y., Hatsukade, Y., Ohtani, T., & Suzuki, S. (2012). Metallic contaminant detection system using multi-channel high Tc SQUIDs. *Journal of Magnetism and Magnetic Materials*, *324*(21), 3487-3490. https://doi.org/10.1016/j.jmmm.2012.02.072.

Tyagi, S., Kumar, A., Singh, M., Sanger, A., & Singh, B.P. (2021). Defects induced photoluminescence and ellipsometric measurements of reactive sputtered growth MoS2 nanoworms. *Optical Materials*, *113*, 110848.

Venimadhav, A., Sher, F., Attfield, J.P., & Blamire, M.G. (2004). Oxygen assisted deposition of Sr2FeMoO6 thin films on SrTiO3 (1 0 0). *Journal of Magnetism and Magnetic Materials*, *269*(1), 101-105. https://doi.org/10.1016/S0304-8853(03)00570-5.

Venimadhav, A., Soukiassian, A., Tenne, D.A., Li, Q., Xi, X.X., Schlom, D.G., Schlom, R., & Ong, N.P. (2005). Structural and transport properties of epitaxial NaxCoO2NaxCoO2 thin films. *Applied Physics Letters*, *87*(17), 172104. https://doi.org/10.1063/1.2117619.

Verna, A., Capelli, R., & Pasquali, L. (2021). Resonant soft X-ray reflectivity in the study of magnetic properties of low-dimensional systems. *Magnetochemistry*, *7*(10), 136. https://doi.org/10.3390/magnetochemistry7100136.

Xu, Z., He, Z., Song, Y., Fu, X., Rommel, M., Luo, X., & Fang, F. (2018). Topic review: Application of Raman spectroscopy characterization in micro/nano-machining. *Micromachines*, *9*(7), 361. https://doi.org/10.3390/mi9070361.

Yadav, A., & Chaudhary, S. (2015a). Effect of growth temperature on structural, magnetic, and transport properties of Co2Cr0. 6Fe0. 4Al Heusler alloy sputtered thin films. *Journal of Applied Physics*, *117*(8), 083911. https://doi.org/10.1063/1.4913516.

Yadav, A., & Chaudhary, S. (2015b). Effect of growth temperature on the electronic transport and anomalous Hall effect response in co-sputtered Co2FeSi thin films. *Journal of Applied Physics*, *118*(19), 193902. https://doi.org/10.1063/1.4935823.

Yasaka, M. (2010). X-ray thin-film measurement techniques. *The Rigaku Journal*, *26*(2), 1-9. https://doi.org/10.1097/01.ss.0000026967.27546.82.

Zhang, X., Tan, Q.H., Wu, J.B., Shi, W., & Tan, P.H. (2016). Review on the Raman spectroscopy of different types of layered materials. *Nanoscale*, *8*(12), 6435-6450. https://doi.org/10.1039/c5nr07205k.